SLAC-J-ICFA-25
Fall 2002
SLAC-R-656

HOME PAGE

http://www.slac.stanford.edu/pubs/icfa/

ICFA INSTRUMENTATION BULLETIN*

The publication of the ICFA Instrumentation Bulletin is an activity of the Panel on Future Innovation and Development of ICFA (International Committee for Future Accelerators).

Volume 25

• Fall 2002 Issue

* Supported by the Department of Energy, contract DE-AC03-76SF00515.

ICFA INSTRUMENTATION BULLETIN

The publication of the ICFA Instrumentation Bulletin is an activity of the Panel on Future Innovation and Development of ICFA (International Committee for Future Accelerators). The Bulletin reports on research and progress in the field of instrumentation with emphasis on application in the field of high-energy physics. It encourages issues of generic instrumentation.

Publisher : Stanford Linear Accelerator Center
SLAC Publications Department
Stanford, CA **94309,** U.S.A.

Editor : J. Va'vra

Web Technical Advisers : J. Schwiening

The views expressed in this Bulletin do not necessarily represent those of the ICFA Panel or the editor. In all cases, the authors are responsible for their manuscripts. The printed version is mailed out in limited numbers to institutions on the SLAC Instrumentation mailing list. Issues of the ICFA Instrumentation Bulletin are accessible electronically on our Web site:

http ://www .slac .stanford.edu/pubs/icfa/

Cover: The illustration depicts L. J. Waghenaer's marine atlas, "The Mariner's Mirror," published in 1588. Lucas Janszoon Waghenaer was born in Holland in the 1530s. He became a famous ship pilot in his time. In 1584, he published the atlas ("Spieghel der Zeevaerdt") which was greatly valued among mariners for centuries. This was not due only to the map content, but also to the detailed knowledge of navigation techniques of that time. The atlas, as it appears on our page, is the same one used for the Dutch to English translation.

Conference List

- The 9-th Pisa Meeting on "Advanced Detectors," La Biodola, Isola d'Elba, May 25-31,2003. Web site: http://www.pi.infn.it/pm/2003/.

- 20032 IEEE Nuclear Science Symposium and Medical Imaging Conference, Portland, Oregon, USA, October 19-25, 2003. Web site: http://www.nss-mic.org.

Table of Contents

CMS HCAL Hybrid Photodiode Design and Quality Assurance Stations

Priscilla B. Cushman and Adriaan H. Heering

University of Minnesota, Minneapolis, MN 55455

***Abstract*- The hadronic calorimeter for the CMS experiment requires photodetection in a 4 Tesla magnetic field. This, plus high neutron radiation and a 25 ns bunch-crossing, necessitated the development of a new type of high-rate multi-channel hybrid photodiode. As our specifications became tighter, design changes in the diode structure and surface treatment became necessary, resulting in a better product with very low crosstalk in both AC and DC modes. The specifications are rigorous and are maintained by a set of automated Quality Assurance stations which will process 570 tubes over 2 years.**

I. Introduction

The CMS Hadronic Calorimeter [1] is a sampling calorimeter composed of scintillating tiles alternating with brass absorber arranged in a projective tower geometry pointing back to the interaction region. Energy deposited in each active scintillator element produces blue light, a few percent of which is captured and re-emitted at ~520 nm in wavelength-shifting (WLS) fibers coiled inside the tiles. Clear fibers mated to the WLS fiber route the light to readout boxes located outside the calorimeter, but still within the 4 T solenoid field. The fibers are originally arranged by horizontal layer, arriving at the reaout box via fiber ribbon cables. They are sorted into bundles corresponding to towers within the readout box itself. The resulting fiber bundles are glued into holes in a black plastic PET (polyethylene terephthalate) disk with 19 or 73 of such bundle holes, each matching the position of an individual pixel on the face of a multi-channel Hybrid PhotoDiode (HPD). The entire assembly is fly-cut and polished, and pressed against the HPD optical faceplate with a spring-loaded, pin-aligned mounting jig as shown in Fig. 1. The bundles can have as few as 2 fibers and as many as 18, depending on the number of tiles stacked into a tower. The readout solution optimized cost per channel by providing 19 and 73-channel HPD's in identical housings and pin-out patterns, though a recent economic measure eliminated the thin compensation layer, and thus the 73-channel (2-3 fibers/bundle) version entirely.

II. Choice of Hybrid Photodiode Technology

The magnetic field constraint forced us to a silicon-based solution. This was quickly narrowed down to 2 possibilities: either a development project using multi-channel HPD's or individual avalanche photodiodes (APD's) of the same type proposed for our electromagnetic calorimeter, producing an integrated readout solution for the combined calorimeter. The decision was made by observing pions, electrons and muons from a tile/fiber calorimeter with both readout systems in a 1995 CERN test beam run [2,3]. The HPD response to MIP's as well as to the DC signal from the radioactive source calibration demonstrated a better signal-to-noise than the APD, despite the better quantum efficiency of the APD. The nuclear counter effect (background caused by muons depositing energy directly in the silicon) is reduced in a hybrid device by the additional factor of gain enjoyed by the photoelectrons of the true signal. Unlike the CMS ECAL which requires compact, individual transducers on each crystal, the HCAL fibers could be arranged in multi-pixel format, leading to a less expensive solution. Since the HPD signal response was uniform over the tube and the current is very low, many channels could be driven by one HV supply and bias. Overall, the HPD system was easier to use, less expensive, and more stable with respect to temperature and bias voltage.

III. Custom Tube Design

A development project was therefore initiated with DEP[1] to produce a tube which fully met the CMS criteria. A photograph of the final tube and internal diode array are found in Fig. 2. The diagram in Fig. 3 shows all the salient

[1] B.V. Delft Electronische Producten, Roden, Netherlands

features of the tube and internal diode in its final form. The following changes to the commercially available 7-channel tube design existing in 1995 were necessary in order to produce this product:

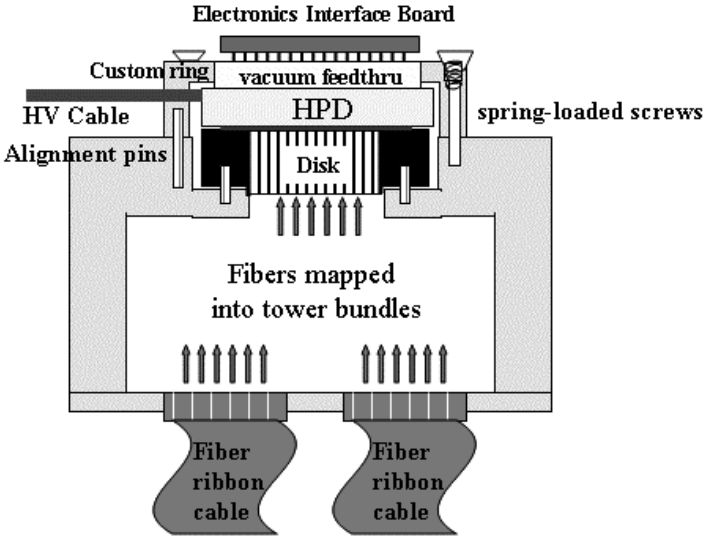

Fig. 1. The HPD is mounted in a readout box which decodes the fibers into tower bundles. The plastic disk which presents the fiber bundles to the HPD faceplate is spring-loaded. Alignment is done during quality assurance, producing custom rings for each HPD, such that the readout box and disk can be universal.

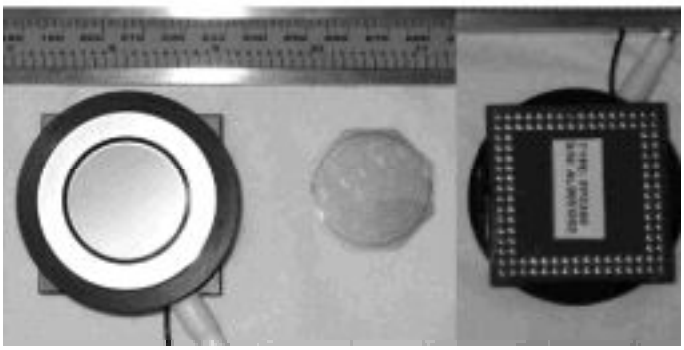

Fig. 2. The front and back of the CMS HPD are shown to the left and right of the 19-channel hexagonal close-packed diode array which is mounted inside.

1) *Reduction in the accelerating gap*

Extensive studies performed in a 5 Tesla, 30 cm bore MRI solenoid confirmed that the tube could handle repeated cycling in the field without damage, despite the presence of the Kovar ring used in brazing the tube [4]. The major effect of an off-axis tilt is a simple image shift due to E x B. Second-order off-axis effects include a cosine reduction in response due to a longer path length through the dead surface layer of the diode (thus raising the effective threshold) [5]. The gap was reduced from 5.3 mm to 3.3 mm to minimize image shift and its size was verified by angular studies in the magnet. A narrower gap relaxed tolerances on alignment of the tubes parallel to the B-field to 2^{o}, such that optical crosstalk due to image shift was eliminated, as long as 400 μm was maintained between the edges of fiber bundles. Even smaller accelerating gaps were rejected as posing too high a risk of high voltage breakdown, since a gain of 2500 requires a 12 kV operating voltage over 10 years of CMS running.

2) *Larger surface area*

The area was enlarged in order to accommodate the larger fiber bundles along with an additional 400 μm of space between bundles. This additional space is needed not only to prevent optical crosstalk between pixels in the event of

a non-parallel alignment of tube axis with magnetic field, but also in order to maintain the mechanical integrity of the plastic disk which presents the fiber bundles to the face of the tube. The 487 mm^2 active area is realized by increasing the window diameter of a nominal 25 mm format tube to 27 mm, putting the perimeter of the active area closer to the walls of the tube than had ever been attempted before, raising concerns about charging of the body walls. Space charge effects were not a problem; instead, the tight space made potting difficult and was responsible for high voltage breakdown in a subset of tubes.

3) *New HV feedthru designs to improve reliability.*

Interior sparking to photocathode can cause sudden death, as well as slow deterioration in photocathode response as pinholes are temporarily created in the fiber optic faceplate, slightly spoiling the vacuum before annealing again. Current spike monitoring stations were developed to detect the onset of sparking before deterioration. They also helped identify the problem, which was then eliminated by potting techniques to reduce voids, and by increasing the insulation between the interior ground and photocathode. The cable sheath is embedded in the tube potting and extends out over the exterior cable in order to provide mechanical support.

4) *Smaller, denser packing of the pixels.*

Optimization of channel cost for the HCAL tower geometry, moderated by the magnetic field tolerances discussed above, led to a close-packed hexagonal array of 5.4 mm flat-to-flat pixels for towers with large bundles (19-channel version) and 2.68 mm flat-to-flat pixels for small bundles (73-channel version). These arrays map to each other in such a way that the same vacuum feedthru design can be used for both, thus reducing the design cost of this component.

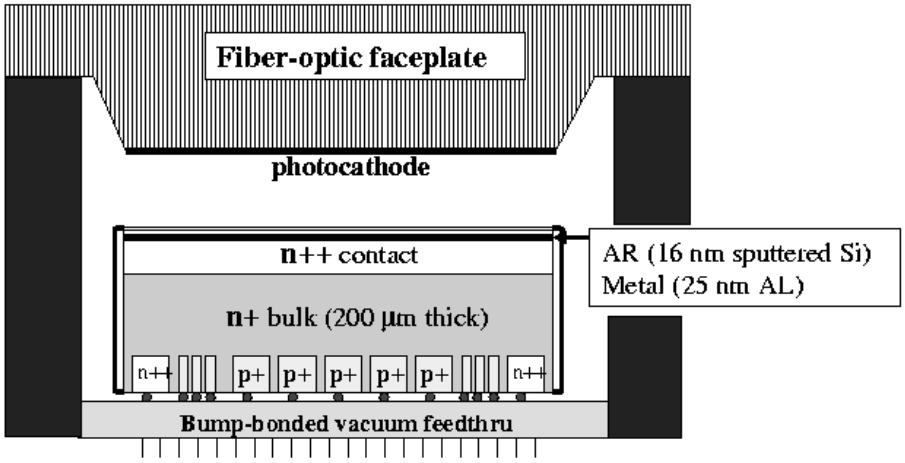

Fig. 3. Representation of the custom CMS diode array internal structure and its installation in a proximity-focussed vacuum tube. Not to scale.

5) *New ceramic vacuum feedthru design*

The 73-channel device required denser pixel arrangements than ever before achieved by DEP. Work sponsored by the SSC project showed that Litton[2] could produce multi-channel hybrid avalanche photodiodes [6] with dense pixel structure by indium bump-bonding to gold pads on a ceramic feedthru. DEP's first tubes were wire-bonded. During the high heat of photocathode processing, several pixels would frequently lose their contact or diffusion of the thin aluminum contact layer into the silicon would cause locally high leakage currents. A failed attempt by DEP to produce their own glass feedthru convinced them to follow Litton's lead. They sub-contracted with Kyocera[3] to design the multi-layer ceramic feedthru, which transfers signals from a hexagonal array of bump-bonds to a standard 0.1" pitch pin grid array (see right-hand photo in Fig. 2). In the assembly of the readout box, these pins fit to a standard zero insertion force (ZIF) socket with a locking lever. In order to assure the reliability of these contacts, the

[2] Litton Electro-Optical Systems, 1215 52nd St., Tempe, AZ 85281, USA
[3] Kyocera Corporation (Fine Ceramics Division), Kyoto, Japan

pins were gold-plated. A study conducted at DEP proved that the diffusion of gold into the Kovar pins during module brazing was not a problem.

6) *Optimization of the photocathode*

An S20 photocathode is applied to a Schott[4] glass fiber optic window (6 μm fibers). The quantum efficiency is 11%-18% at 520 nm with a broad wavelength maximum. Care is taken to keep the red sensitivity low since this translates into increased dark counts. Tubes have dark counts at rates from 0.5 kHz/cm^2 for quantum efficiencies of 0.2% (800 nm) up to a MHz/cm^2 for one tube with 2.8% (800 nm) quantum efficiency.

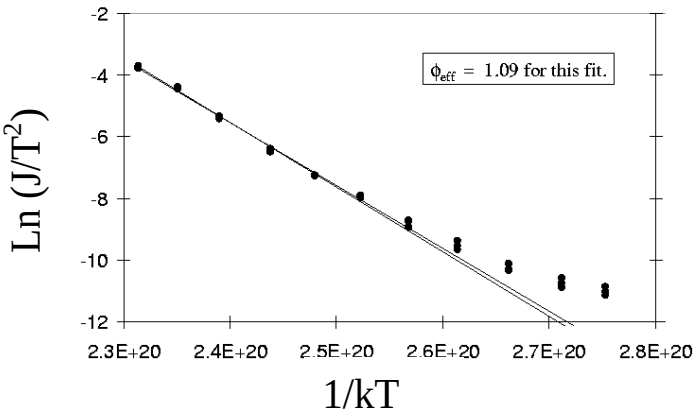

Fig. 4. The number of individually counted dark counts per pixel from the photocathode of a sample 73-channel HPD as a function of temperature, plotted such that the slope gives the work function according to the Richardson-Dushman equation. Several runs were taken and the fits are also shown.

Work functions, Φ, of the photocathodes were obtained by fitting the Richardson-Dushman equation [7]:

$$J(T) = A\,T^2 \exp(-\frac{\Phi_{eff}}{kT})$$

where T is the temperature, k is the Boltzmann constant, A=1.2x10^6 A/m^{2}K^2 is the Richardson constant and J(T) is the dark current density. The work function is extracted from Φ_{eff}

$$\Phi_{eff} = \Phi - \sqrt{Ee^3/4\pi\varepsilon_o}$$

where the applied field E = 2750 kV/m and e is the electron charge. Fits were performed for photocathodes at temperatures down to –10° C using an aluminum box coupled to a Peltier cooler, finding Φ of 1 to 1.33 eV. Micro-sparking in earlier tubes produced a departure from the Richardson-Dushman equation at low temperatures, representing a constant, low background. The sparks produced light (as measured by a PMT pressed against the HPD faceplate), the rate of which depended on the applied high voltage.

IV. DIODE DESIGN

The silicon diode is fabricated using epitaxial growth by Canberra[5] with the basic structure outlined in Fig. 3. The photoelectrons are converted to electron-hole pairs within the first few micrometers of the surface of the lightly-doped (n+) bulk n-type layer. The holes drift through the silicon and are collected from the backside p+ implants, which define a hexagonal close-packed array of pixels. Additional p+ structures on the back define a grounded ring plus six floating guard rings that maintain uniformity for the edge pixels and aid in maintaining a high breakdown voltage. At the edge of the diode, there is an n++ ring, which supplies the bias voltage from the back of the diode to the front n++ surface through the bulk material. There are 40 microns between each pixel implant, but no dead space in the response uniformity.

[4] Schott Fiber Optics Inc, 122 Charlton St, Southbridge, MA 01550, USA
[5] Canberra Semiconductor N.V., Lammerdries 25, B2250, Olen, Belgium

The shape of the output pulse in response to a delta function input pulse, reveals much about the internal structure of the diode. The rising and falling edges are defined by the RC constant of the combined diode plus preamplifier and connections, whereas the central region is determined by the drift speed of the holes [8]. Thus, the slope of the mid-region of the pulse shape mirrors the internal E-field generated within the diode as a function of x through the bulk in our simple model, similar to treatments for silicon trackers [9]:

$$E(x) = \frac{2V_d\, x}{d^2} + \frac{(V_b - V_d)}{d}$$

where d is the diode thickness, V_d is the depletion voltage, and V_b is the applied bias. Integrating to get the current:

$$I(t) = e^{\frac{2\mu V_d}{d^2}t}\, Nq\mu(V_b - V_d)/d^2$$

where Nq is the total charge generated within the depleted region and μ is the hole mobility, μ.= (1/E) dx/dt = 450 cm^2/Vs. The plateau of the pulse is flat for low depletion voltages or thick diodes, where the exponent in the current is small. The output current pulse has a width given by the time Δ(ns) for a hole to travel distance d:

$$\Delta(ns) = d^2\, \ln\left(\frac{\sqrt{V_b + V_d}}{\sqrt{V_b - V_d}}\right)/\mu V_d$$

In Fig. 5, scope traces of the response to a 1.5 ns pulse from a light-emitting diode (LED) show how the structure of the diode has changed over our development period. The conventional 300 μm thick silicon gave wider than optimum pulses for the CMS application. Reversing the diode doping scheme in order to drift the faster mobility electrons would have necessitated a new (and expensive) development project with Canberra, so instead, we decided to reduce the wafer thickness to 200 μm in order to reduce d in the above equations. Despite the increased fragility of the wafers, the loss in yield has been negligible.

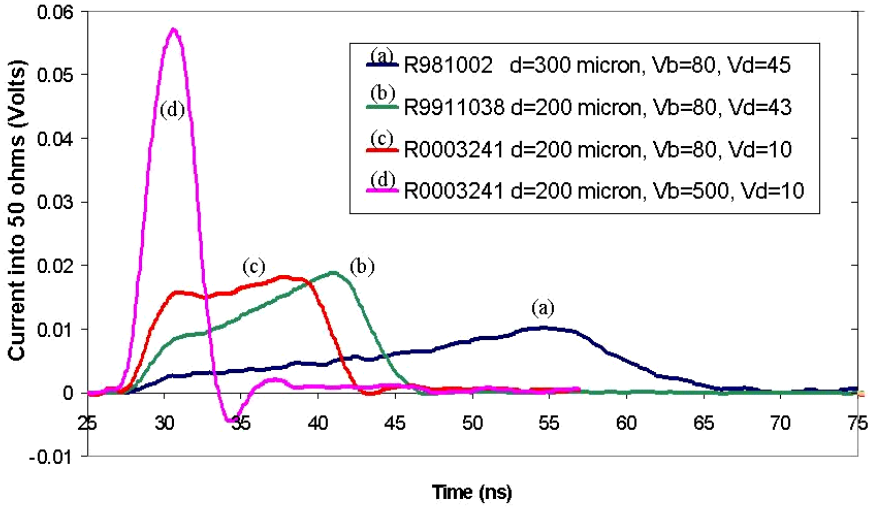

Fig. 5. Pulse shapes for (a) the 300 micron and (b) the 200 micron diodes at 80 V bias, (c) the low-depletion, 200 micron diodes at 80 V bias and (d) the low-depletion, 200 micron diodes at 500 V bias.

A further improvement in pulse width can be obtained by insisting on higher resistivity silicon, which pushes down the depletion voltage. In Fig. 5, the pulse shapes from later diodes (c) clearly show a flatter plateau and narrower width at the operating voltage of 80 V. Once the depletion voltage is small compared to the bias, the output pulse becomes square with its width $\Delta(ns) \sim d^2/\mu V_b$ and its height maintaining the total area via $h(nA) \sim Nq/\Delta$. The later diodes were also able to tolerate much higher reverse bias without breaking down, and so could be operated in a highly depleted mode: see the very narrow pulse (d) in Fig. 5 at a bias of 500 V.

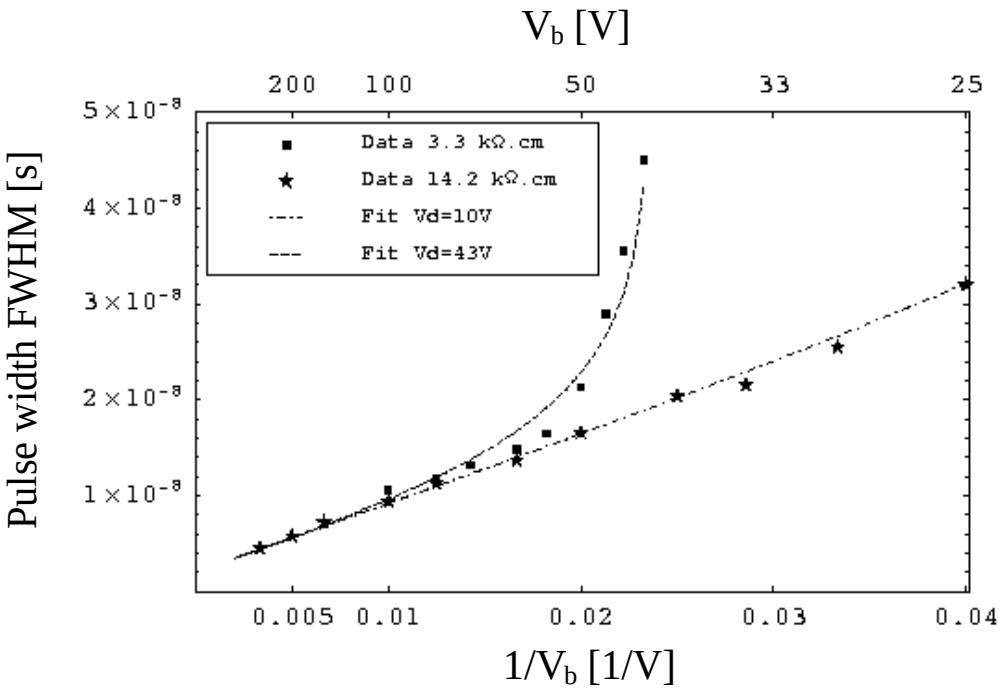

Fig. 6. Pulse width versus inverse bias voltage. Data (squares) from the earlier diodes fitted to the above model for pulse width, shows that the width diverges quickly below the operating bias of 80 V, whereas the new diodes (stars) with lower depletion voltage have a 'linear' behavior as the voltage is decreased.

Using the above model, fits to the pulse width as a function of inverse applied bias in Fig. 6 show that the low depletion diodes produce stable pulse shapes at the operating bias voltage of 80 V, whereas higher depletion voltages can be affected by variations in the delivered bias. We therefore specified a minimum resistivity of 5 k**Ω**-cm, corresponding to $V_d < 30$ V for d = 200 μm and an electron mobility (according to Canberra) of 1350 cm^2/Vs. We specify a maximum depletion voltage of 35 V to accommodate the tolerance in the diode thickness. The capacitance per pixel when depleted is measured to be <5 pF/pixel for the 73-channel device and 16 pF/pixel for the 19-channel diode.

V. CROSSTALK

1) AC Capacitive Crosstalk

As work progressed on implementing the fast electronics required for the CMS readout, we discovered differential crosstalk between pixels that depended on the speed of the charge integration. This was not noticed when using the slower preamplifiers and gated ADC's of the test beam. The 300 ohms/sq resistivity across the 100 nm thick upper n++ layer and the 300 ohms resistance from back n++ bias contact to the front, provided insufficient current to respond to the faster pulses and shorter integration time, thus draining the neighboring pixels. A large negative-going pulse in Fig. 7(b) is induced in a side pixel of the bare silicon 19-channel HPD when the central pixel (the positive trace (a) shown at 1% of its actual size) is illuminated. There is not much radial dependence in this differential crosstalk, so that even though it is only 2.5% per pixel (1% per pixel for the 73-channel tube), it adds up to 50 % over the whole tube. This is AC crosstalk, in that it only shows up for fast pulses and has its largest effect on tube performance in high rate experiments.

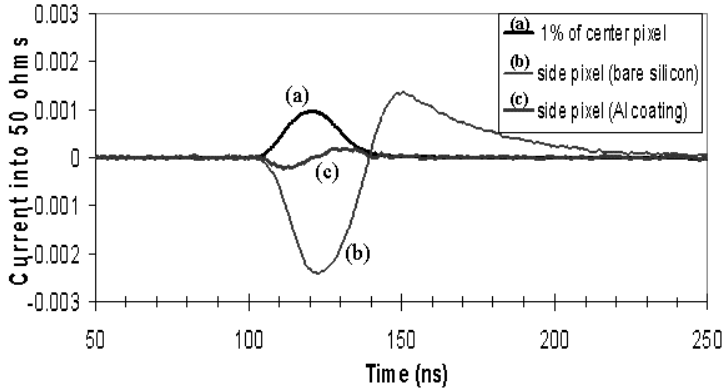

Fig. 7. AC cross-talk observed in (b) the side pixel of a bare silicon 19-channel HPD when (a) the input signal is in the center pixel. Reduction of this component for the aluminized HPD is also shown in curve (c).

The AC crosstalk was reduced to < 4% over the whole tube by applying a thin (25 nm) aluminum layer over the entire front surface. This reduced the resistivity to ~1 ohms/sq. Conduction was extended to the back bias contacts via 100 nm thick aluminum traces at two edges of the diode. After high leakage currents in some diodes indicated that diffusion of aluminum into the silicon was occurring during module brazing, a SiO_2 barrier layer was introduced between them. This barrier layer meant there was no longer a direct contact between the aluminum and n+ layer, but the capacitive coupling was sufficient to maintain charge delivery to the individual pixels at high rate operation and the leakage current drained through the bulk silicon. Canberra also demonstrated low leakage currents without a barrier layer by doping the aluminum itself with 1% silicon. The middle trace (c) in Fig. 7 demonstrates how the AC crosstalk has been made negligible by the aluminization.

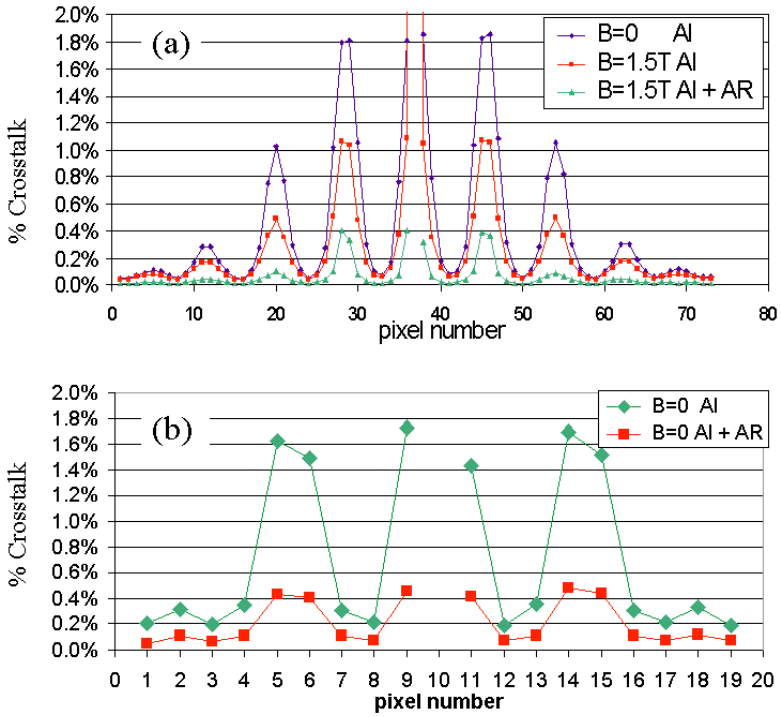

Fig. 8. (a) The combined backscatter and optical crosstalk (B=0) across an entire 73-channel HPD compared to the remaining optical reflection crosstalk once the field is turned on (B=1.5 T). The lowest crosstalk is for the tube with an anti-reflective coating over the aluminized layer. Light is injected into the central pixel, number 37. (b) The combined crosstalk (B=0) across a 19-channel HPD for the aluminized tube compared to the backscatter-only crosstalk once the anti-reflective (AR) coating has removed the optical component.

2) Optical Crosstalk

Removing the negative AC crosstalk revealed positive crosstalk which had previous been masked by the AC effect. Ironically, that positive crosstalk had been worsened by the addition of aluminum. If this crosstalk is caused only by backscattered electrons, then it can be eliminated by applying an axial magnetic field above 1 Tesla, since at that field strength, all electrons are focused back into the same pixel. As can be seen from the second curve in Fig. 8(a), a 1.5 T field has improved the situation, but there is still a low level of positive crosstalk remaining. This turns out to be light which is not converted by the photocathode. It reflects off the front surface of the diode, cannot be focused by the magnetic field, and has a second chance to produce photoelectrons when it again strikes the photocathode far from where it first entered. It is this optical crosstalk which is most adversely affected by the increased reflectivity of aluminum.

The radial dependence (Fig. 9) of the crosstalk in the first production 19-ch HPD was mapped by moving an illuminated 250 μm fiber across one pixel and reading out the adjacent pixel. In these plots, the origin corresponds to the pixel boundary and the value at 2.7 mm means that the fiber is in the center of the illuminated pixel. The B=1.5 T case represents almost purely optical crosstalk, shown in Fig. 10 as a fraction of the central current. No data at <0.5 mm is conclusive because a 1.5 T field with a back-scatter radius of 0.5 mm is used to subtract the optical component. In any case, no fiber will ever be closer than 0.8 mm to the boundary due to the construction of the cookies.

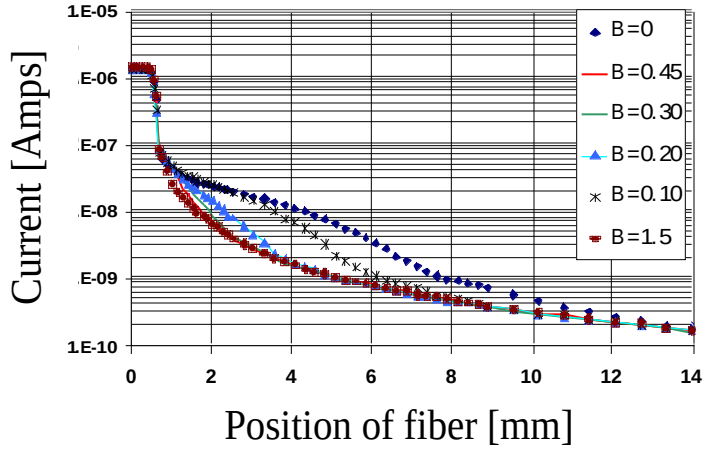

Fig.9 Raw crosstalk data for HPD AZ0139031

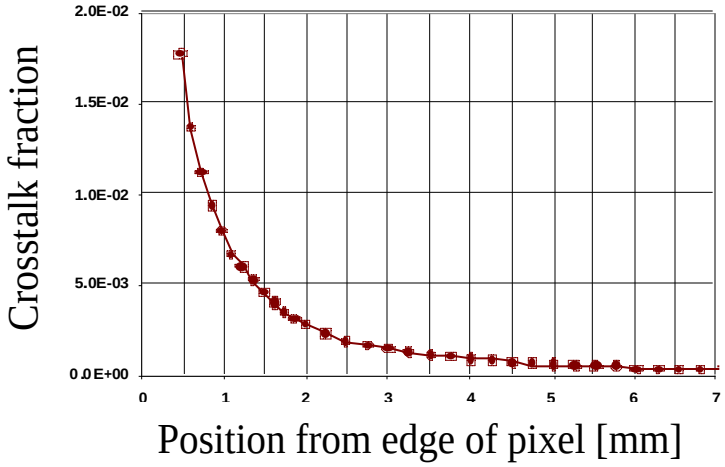

Fig. 10 Optical crosstalk component from 2nd bounce photoelectrons

The optical crosstalk curve was found to be completely consistent with a direct measurement of the reflected light off the internal diode using an avalanche photodiode on the surface of the HPD fiber optic faceplate, confirming that optical reflection is indeed responsible for crosstalk which survives in the presence of a high magnetic field. An interesting aside is that presumably all hybrid silicon devices have reflection crosstalk, since the reflectance of bare silicon at 40% is still significant, compared to 90% for our aluminum coating. This means that the true quantum efficiency of even a single channel HPD is less than the effective quantum efficiency, since the measured value always includes the reflection enhancement.

3) Back-scatter Crosstalk

By subtracting the B=1.5 T data (optical component) from all lower B-field data, we obtain the pure back-scatter distributions in Fig. 11. Since the radially symmetric back-scatter dependence is convoluted with an hexagonal pixel shape, the slope discontinuities represent true geometric effects.

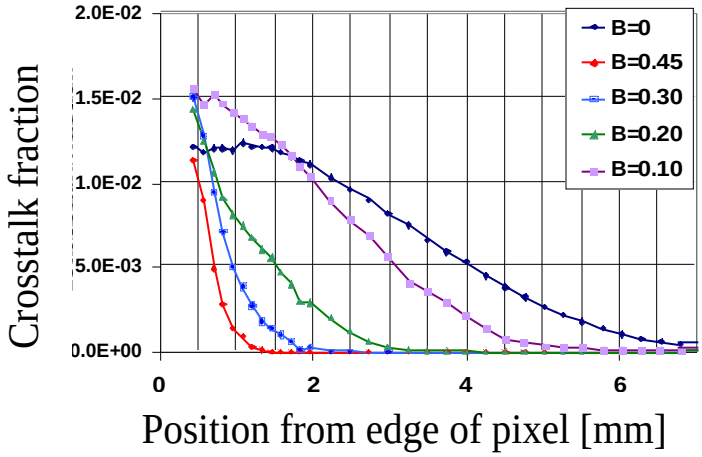

Fig. 11 Radial distribution of back-scatter crosstalk

From the Darlington paper [10], we expect 18% of the 10 keV electrons to be back-scattered with an average energy of 7 keV. The radial distance to impact point is dependent on the initial back-scattered angle: for B = 0, the maximum distance is when the initial angle is at 45 degrees and is given by 2d = 6.7 mm where d is the accelerating gap between photocathode and diode. For B=0.2 T and an initial angle of 0.65 radians, the electron comes back to the same place (radial distance = 0) after making one turn. For higher fields this becomes a spiral of multiple turns, thus causing multiple zeros, representing the particle returning to the origin. The radial intensity (Fig. 12 below) comes from this simple model

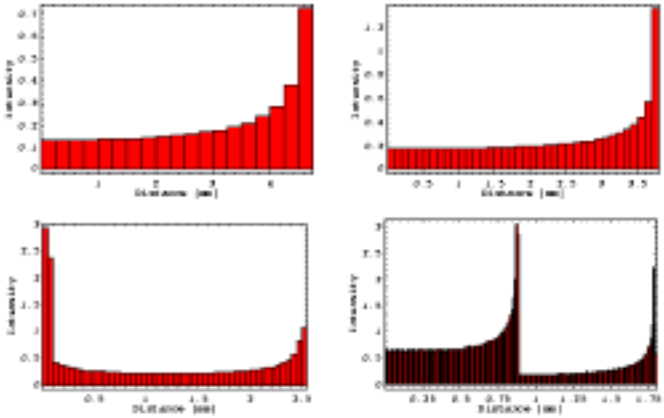

Fig.12.Balllistic Monte Carlo of radial back-scatter intensity for 7 keV electron at fields of B=0.0 T, B=0.1 T, B=0.2 T, B=0.3 T.

For B=0, this represents a fairly uniform disk of back-scatter (once the area of each increasing annulus is accounted for, as well as the blurring due to a range of energies) extending out to 5 mm on average (out to 6.7 mm for the max 10 keV). As the field is turned on, the disk shrinks and eventually at B = 0.2 T gets a second spike in the center from particles returning to the origin. Since the rim remains, however, moving a fiber slightly off-center results in a large increase in total crosstalk. When the field is off, the back-scatter disk is much larger than the pixel size and back-scatter crosstalk will be insensitive to where a fiber is located. Thus, fields of 0.1 T can actually be worse than no field at all, since crosstalk will now depend on which fiber in the bundle is lit up, whereas with zero field, the crosstalk is uniform and can be corrected by a simple factor.

VI. ANTI-REFLECTIVE COATING

In order to eliminate crosstalk due to reflection, we studied how to apply an anti-reflective coating to the front surface of the aluminum. We studied several options, including replacing the aluminum with silver, which would have provided both anti-reflection and AC crosstalk elimination in one thin layer, but oxidation made it far less stable. Other solutions with multiple metal layers produced unacceptably thick dead layers, thus increasing our threshold voltage and reducing our gain. Our choices were guided by an optical modeling package for multilayer structures called IMD[11]. In general, the thickness of the layers determines at which wavelength the minimum occurs, and the composition of the material determines the width and strength of the minimum. Our optimized formula called for 14 nm of hydrogenated amorphous silicon (a-Si:H) deposited over 25 nm of Al with a native layer of Al_2O_3 in between.

We made a series of test slides by plasma-enhanced chemical vapor deposition of a-Si:H (approximately 4% H by atomic weight) on glass slides with an initial 25 nm coating of aluminum. The thickness of the amorphous silicon layer was determined by varying the exposure time and comparing the resulting wavelength minimum with simulations using IMD. The slides were illuminated through a monochromator of 4 nm bandwidth. The reflected light was observed with a PIN diode in order to measure the reflectance as a function of wavelength and angle. The diode itself was also illuminated in the same position as the slide, and its wavelength response divided out. The system properly observed a flat response from a 99% reflectivity mirror and from the bare aluminized slide. The wavelength of the monochromator was checked with a calibrated filter. Our films matched the modeling program very well, as can be seen in Fig. 13.

DEP then tried to apply the same coatings, using a sputtering technique and non-hydrogenous amorphous silicon. Our calculations predicted that they should use 16 nm of a-Si to achieve the same wavelength minimum as 14 nm of a-Si:H. We measured their samples in the same setup used for our slides. Since their results depend on pressure, as well as other variables, it has been harder to come to a consistent picture. However, the DEP curve also shown in Fig. 13 can be reliably reproduced by DEP and provides adequate reduction in optical crosstalk at 520 nm. The thin layer of Al_2O_3 between aluminum and a-Si coating stabilizes the coating, which otherwise tends to disappear during tube processing via diffusion. In the end, it was unnecessary to apply this as a coating: merely exposing the aluminum surface to air for a short time was sufficient to create a native layer of Al_2O_3.

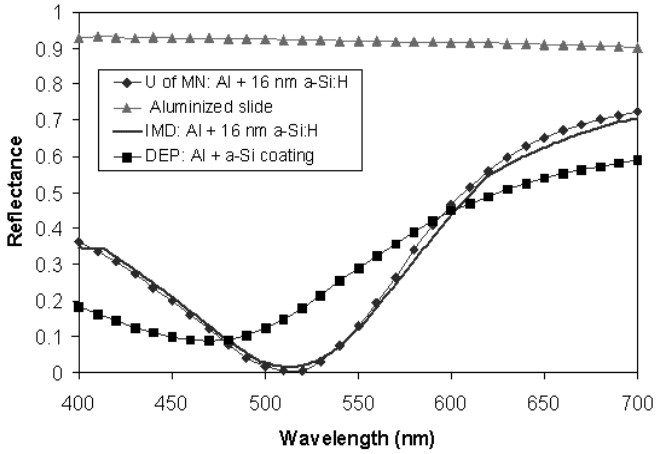

Fig. 13. 14 nm of a-Si:H deposited by PECVD on aluminized glass slides matches the IMD optical modeling program. The bare aluminized slide has an approximately flat response at 92%. The DEP sputtered a-Si, with a minimum of 475 nm gives adequate reflection crosstalk reduction, but could be better optimized.

Our success is measured in the crosstalk reduction finally obtained, for an acceptable increase in the thickness of the dead surface layer. After all surface treatments, the threshold voltage deduced by extrapolating the linear portion of the gain curve back to where it crosses the x-axis (see Fig. 20) went from a range of 500-1500V to 2000-2500V. The true threshold is overestimated by this procedure since a shallower slope in the gain is masked by an upturn in the quantum efficiency with voltage. The lowest curve in Fig. 8 (a) shows that the crosstalk in a 73-channel aluminized tube with anti-reflective coating is only 0.4 % into the nearest neighbors when the B-field removes the back-scatter component. It goes down to 0.1% at the next-nearest neighbors, which correspond to the nearest neighbors in the 19-channel tube. Fig. 8(b) shows the zero magnetic field case for the 19-channel tube, where back-scatter still contributes. The bottom curve shows the improvement due to the AR coating on that tube, effectively removing the optical component from the total crosstalk.

One can summarize the situation in Table I by quoting the total crosstalk in the whole tube. Recall that the crosstalk into any neighbor is below one percent, but the definition of "crosstalk" in Table I is the total amount of energy removed from the illuminated pixel into all other pixels. The components due to optical reflection and electron back-scatter can be isolated by making the same measurements in and out of a magnetic field. Since we operate at 4 T, the back-scatter component will be removed from consideration in the actual experiment, so the total crosstalk we will observe is within specifications and measured as 2-4%.

TABLE I: CROSSTALK
Percent removed from central pixel into all other pixels

Diode Type	Total % (B=0)	Optical % (B=1.5 T)	Backscatter % (B=0 – 1.5 T)
73-ch HPD			
Bare Silicon	18	7	11
Si + 25 nm Aluminum	29	16	13
Si + SiO_2 + Al + a-Si	10.4	2.4	8
19-ch HPD			
Bare Silicon	13.4	4.8	8.6
Si + SiO_2 + Al + a-Si	8.5	2.1	6.4

VII. QUALITY ASSURANCE

The final specifications are detailed in the contract with DEP (see Table II). The vendor is responsible for providing data on specifications 1, 4, 11, 12, 14, 15, 20, 21, 22. When the tubes arrive at the University of Minnesota, they are held for two weeks at 13 kV while current from the supply is monitored for sparking. Next the tubes go through an automated scanning station at a rate of one tube every 6 hours, transferring data to the CMS database on items 3, 5, 8, 10-17. Item 23 is checked with a Go/NoGo mechanical jig.

Besides uniformity scans, gain curves and leakage current maps, the scanning station also registers the position of the pixels within each HPD to 50 μm. An attached metal strip with 3 precisely-positioned 1 mm holes provides fiducial spots on the surface of the HPD when the focussed beam of light strikes the holes. The moveable platform translates the mounted HPD assembly in steps of 0.1 mm in x and y, to find the center of the light spots. These are then registered to the pixel intersection positions (above and below the metal strip in the same scan) via an automated iterative procedure using pixel response equalization. This provides a set of corrections in Δx, Δy, and θ to the standard mounting, which can then be used in machining the square hole in the mounting ring (see Fig. 1) which precisely registers the vacuum feedthru, and thus the tube as a whole. In this way, the disks, which hold the fiber bundles are simple inserts to the custom mounting ring and can be prepared ahead of time in batches and sent out to other institutions for fiber gluing, fly-cutting and assembly. A capacitance station measures capacitance and resistance as a function of bias voltage to determine the quality of the silicon and the depletion voltage, items 10-13.

TABLE II
SPECIFICATIONS FOR THE CMS HPD

PHOTOCATHODE (multi-alkali, glass FO)	*MIN*	*TYP*	*MAX*	*UNIT*
1. Quantum efficiency at 520nm	11	14		%
2. Dark counts			50	kHz/cm^2
3. Response non-uniformity			8	%
4. Operating voltage		12	13	-kV

PIN DIODE ARRAY	*MIN*	*TYP*	*MAX*	*UNIT*
5. Threshold for 10kev e$^-$	500	2500	3300	V
6. Thickness non-uniformity			±1	μm
7. Silicon resistivity	5			kΩ-cm
8. Response non-uniformity			10	%
9. Inter-pixel resistance	100			MΩ
10. Depletion depth	185	200	215	μm
11. Operating voltage	80	80		V
12. Breakdown voltage	100	150		V
13. Full depletion voltage		10	35	V
14. Guard ring reverse current			500	nA
15. Pixel reverse current		1	10	nA

TUBE PERFORMANCE	*MIN*	*TYP*	*MAX*	*UNIT*
16. Gain	2300	3300		e/pe
17. Gain non-linearity (1 - 70000 pe's)			5	%
18. Total optical crosstalk to sum of all pixels			4	%
19. Total capacitive crosstalk to all pixels			3	%
20. Full width half max at 80 V			20	ns
21. Baseline signal width maximum at 80 V			30	ns
22. Gap between photo-cathode and diode			3.55	mm
23. Carrier size tolerance within one batch			±40	μm

The tubes then undergo tests with pulsed light. Items 20-21 are addressed by observing sample pulse shapes and item 19 is addressed by an AC crosstalk test which compares the pulse in the illuminated pixel to 2 side pixels to determine if the aluminized coating and traces are thick enough (the resistance test also confirms this). Item 2 is addressed by taking pulse height spectra at low light levels using two 32-channel preamplifiers[6] serially read out through a voltage-sensing ADC. The microsecond shaping time gives individual photoelectron peaks, so that ion feedback or problems with the tube vacuum are easily flagged by observing the shape of the spectral tails. Optical crosstalk (item 18) is tested by measuring the current in all surrounding pixels when the central one is illuminated. The HPD is sandwiched between two disk magnets with a 0.3 T magnetic field, on order to remove the back-scattering component. A typical tube is characterized in Figures 14-21 in order to demonstrate the data which is available through the quality assurance system. These plots come directly from the maintained database and will eventually represent the largest statistical sample of HPD's ever characterized, helping to define yield and reliability for future experiments.

Selected tubes from each batch undergo lifetime testing after which the quality assurance procedure is repeated. The tubes must be able to operate for 10 years in a radiation field (mostly MeV neutrons), as well as handle integrated charge over that period as high as 3 C/pixel (off the anode) over a large bundle illuminating a 19-channel pixel at the most forward part of the barrel region [12]. Two 1 mm diameter WLS fibers are excited by blue LED's and read out on one end by calibrated reference PIN diodes. The other end is potted into a cookie and retracted slightly from the HPD window such that the entire pixel is illuminated. The LED's are set, one to deliver the maximum expected CMS charge in 10 months and the other to run at 1/10 the rate. The current from both reference diodes and the two HPD channels, as well as the temperature, are continuously monitored at time intervals of 30 minutes. In all 4 of the tubes observed so far, there is an increase in the effective quantum efficiency for the first 100 mC of charge, after which the response falls off at less than 1% per CMS year. Current spikes of greater than 100 nA will also trigger a reading in order to determine if internal sparking occurs. We also monitor the current off the high voltage supply.

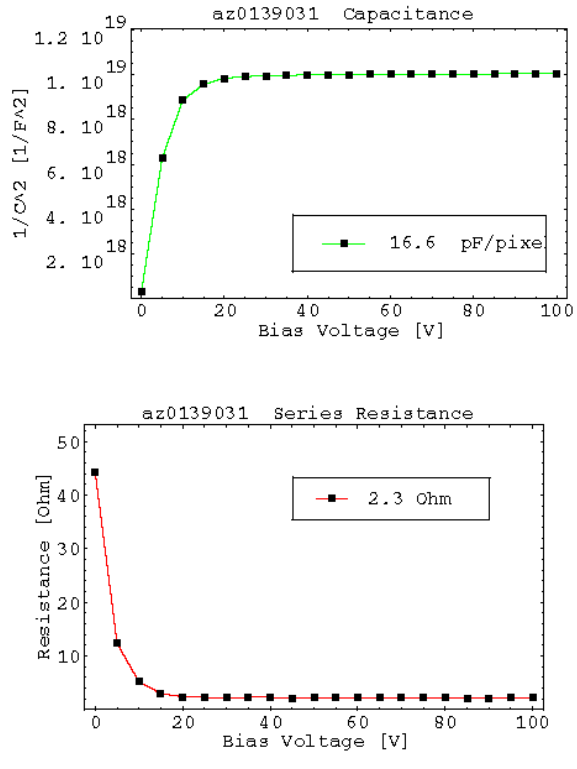

Fig. 14 Diode characterization in Capacitance Test Station

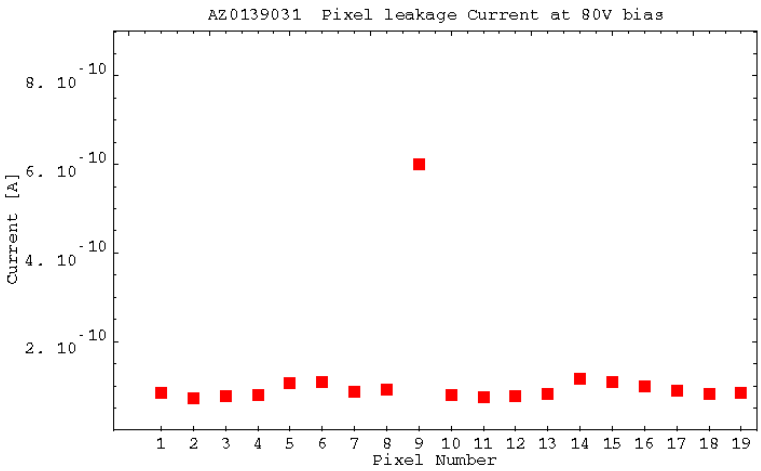

Fig. 15. Leakage Current per pixel at 80 volt reverse bias

A duplicate of this station resides outside a retractable drawer of the University of Minnesota Californium-252 irradiation facility. Quartz fibers link the LED-stimulated WLS fibers to the HPD inside the MeV neutron field and continue to monitor the tube response in situ as exposure proceeds. Radiation damage produces an increase in leakage current proportional to the dose. The aluminized 73-channel tube behaved in the same way as earlier tubes

[6] VA-Rich Viking chip. IDEAS, Hovik, Norway. http://www.ideas.no

[13]. Although the temperature was monitored, it was unnecessary to correct for it inside the thermally insulated concrete pile that houses the source. After a small increase in effective quantum efficiency, the main effect was an increase in leakage current corresponding to 50 nA over 4.5 x 10^{11} n/cm^2 effective integrated dose. The 19-channel pixels expect a factor of 4 more due to their larger area. The dose corresponds to approximately 100 CMS years in the worst section of the barrel.

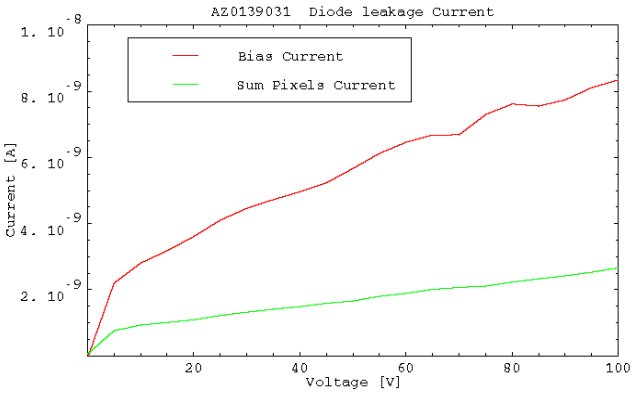

Fig. 16. Leakage current as a function of the bias voltage off supply (includes guard ring) and pixels tied together.

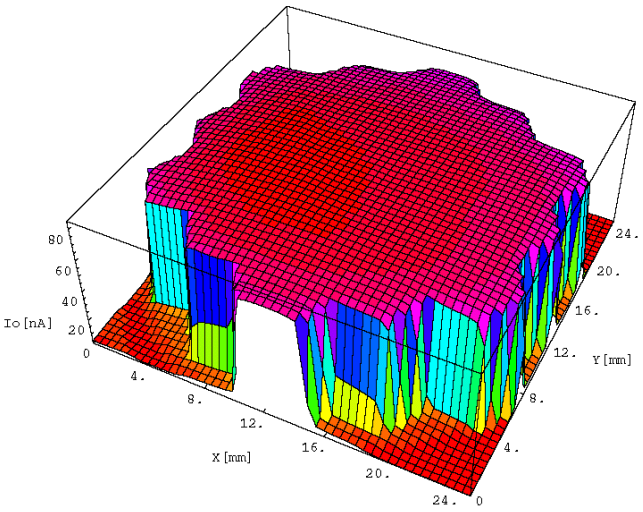

Fig. 17. DC scan of 19-ch HPD. No dead areas between pixels.

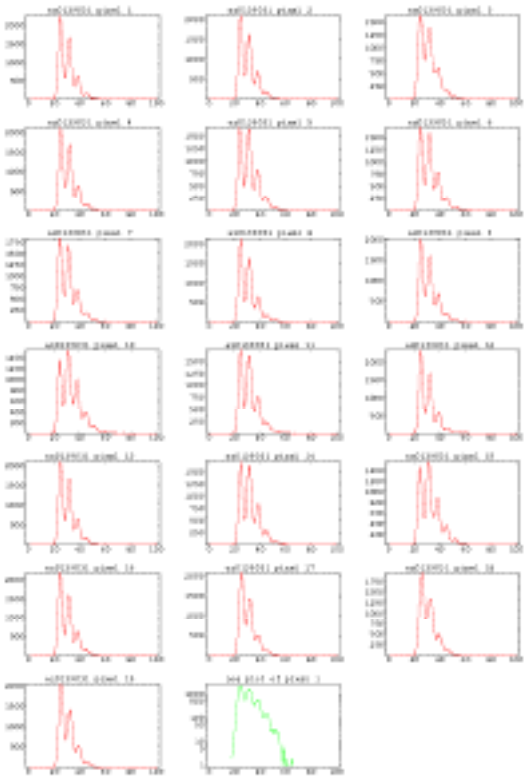

Fig. 18. Individual pulse height spectra for each channel and for the sum at low light levels. Viking AC setup.

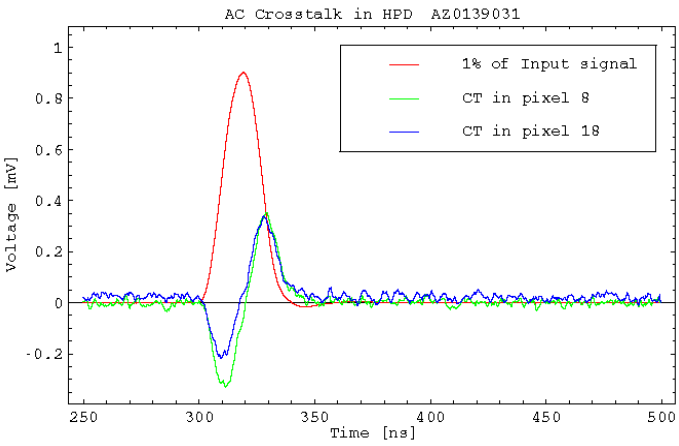

Fig 19. Capacitive AC crosstalk in selected pixels compared to 1% of actual signal in illuminated middle pixel.

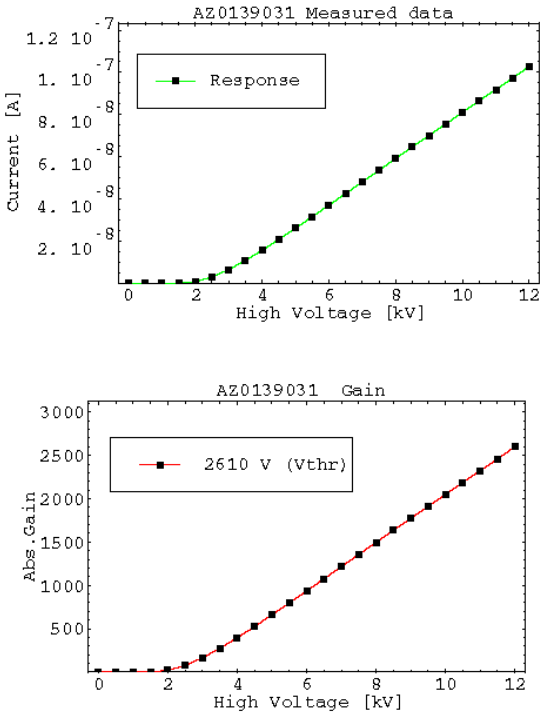

Fig. 20. Response curve and extracted absolute gain curve with, extrapolated threshold voltage. Since the quantum efficiency actually goes up with HV, the threshold is overestimated.

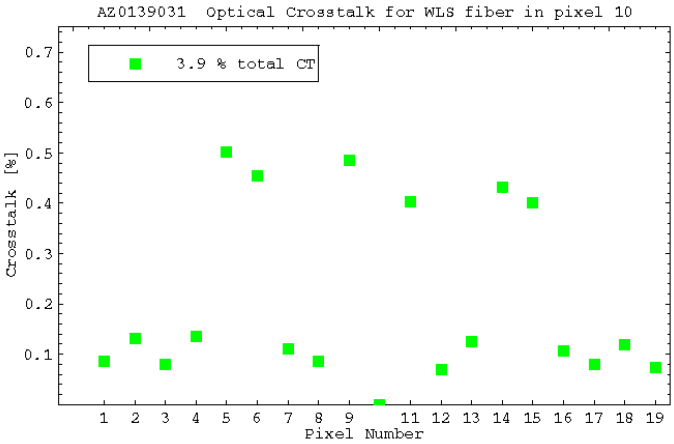

Fig. 21. Optical Crosstalk per pixel when central pixel is illuminated. DC test in a 0.3 T magnetic field.

VII. Acknowledgment

We thank Anatoly Ronzhin and Sergey Los for many interesting discussions, as well as the support of the entire US-CMS HCAL collaboration. We thank Bruce Hammer for the NMR magnet facility at the Center for Industrial Applications of Magnetic Resonance, Univ. of Minnesota. This work was supported in part by the U.S. Department of Energy under Grant DOE/DE-FG02-94ER40823

VIII. References

[1] CERN/LHCC 97-31, CMS TDR 2, 20 June 1997

[2] P. Cushman, A. Heering, J. Nelson, C. Timmermans, S.R. Dugad, S. Katta, S. Tonwar, "Multi-pixel hybrid photodiode tubes for the CMS hadron calorimeter," Nucl. Instr. Meth. vol. A387, pp. 107-112, 1997.

[3] V. V. Abramov, B. S. Acharya, N. Akchurin, A. Ball, S. Banerjee, P. de Barbaro, et al., "Studies of the response of the prototype CMS Hadron Calorimeter, including magnetic field effects, to pion, electron, and muon beams," Nucl. Instr. Meth. vol. A457, pp. 75-100, 2001.

[4] P. Cushman, A. Heering, and A. Ronzhin, "Studies of hybrid photomultiplier tubes in magnetic fields up to 5 Tesla," Nucl. Instr. Meth. vol. A418, pp. 300-305, 1998.

[5] G. Anzivino, H. Arnaudon, P. Baillon, P. Benetti, L. Boskma, P. Burger, et al. "Review of the Hybrid photo diode tube (HPD) an advanced light detector for physics," Nucl. Instr. Meth. vol. A 365, pp. 76-82, 1995.

[6] P. Cushman and R. Rusack, "A photomultiplier tube incorporating an avalanche photodiode," Nucl. Instr. Meth. vol. A333, pp.381-390, 1993.

[7] A. Modinos, "Field, Thermionic and Secondary Electron Spectroscopy," See p.20, p. 40 (Plenum, 1984)

[8] P. Benetti, C. Cattaneo, R. DeSalvo, V. Filippini, D. Grassi, M. Rossella, et al., "Speed properties of the hybrid photodiode tube," Nucl. Instr. Meth. vo.l. A367, pp. 384-387, 1995.

[9] G. Lutz and A. S. Schwarz, "Silicon Devices for Charged-Particle Track and Vertex Detection," Ann. Rev. Nucl. Part. Sci., vol. 45, pp. 295-335, 1995.

[10] E. H. Darlington, "Backscattering of 10-100 keV electrons from thick targets," J. Phys. D 8, pp. 85-93, 1975.

[11] IMD Version 4.1.1, optical modeling package for multilayer structures by David L. Windt, http://cletus.phys.columbia.edu/windt/idl .
[12] P. Cushman, A. Heering, and A. Ronzhin, "Custom HPD readout for the CMS HCAL," Nucl. Instr. Meth. vol. A442, pp. 289-294, 2000.
[13] P. Cushman, A. Heering, and J. K. Nelson, "The effects of neutron irradiation on multi-pixel hybrid photodiode tubes," Nucl. Instr. Meth. vol. A411, pp. 304-312, 1998.

Technology Developments for Deep Underwater Neutrino Telescopes

G. D. Hallewell[+]
Centre de Physique des Particules de Marseille (CNRS/IN2P3), France

Abstract

The July-2002 report of the High Energy Neutrino Astrophysics Panel (HENAP, [1]) recommended the construction of a km^3-scale Northern hemisphere neutrino observatory to complement a large-scale under-ice observatory (IceCube) in the Southern hemisphere. Such an observatory would study cosmic neutrinos with energies in excess of a few hundred GeV, which arrive undeviated from a variety of galactic and extragalactic sources of astrophysical interest, and which might be produced in the possible annihilation of dark matter particles, including neutralinos.

Future developments in technology from that being presently implemented by the Lake Baikal, Nestor, and Antares collaborations toward that necessary for a much larger km^3-scale array are discussed. In January 2000, a part of the Nemo collaboration, engaged in studies for a km^3–scale detector close to the Sicilian coast, joined Antares in the development of a $0.1km^2$ detector. The two collaborations have formed a common working group to coordinate the effort toward the construction of a km^3- scale detector.

The great depth presents numerous technical challenges in the construction, deployment and interconnection of such detectors, and may require the involvement of industrial contractors with experience in fields including deep-sea oil exploitation, submarine telecommunications cable deployment, underwater acoustic navigation and communication, and in the operation of manned or remotely-operated submarine vehicles. This paper reviews the status of some of the technologies for underwater neutrino detector arrays.

(1) Introduction and detection principles

Most of the existing models for neutrino production in astrophysical sources estimate from a few to tens of events per year in a ~ km^2 aperture detector for energies >1TeV. By concentrating the detection upon upward-going neutrinos originating in the hemisphere on the opposite side of the Earth to a deeply immersed detector, the Earth is used as a shield against cosmic ray induced background. Only a Northern hemisphere detector is capable of seeing such neutrinos from point sources in the central region of our galaxy.

Many of the principal characteristics of an underwater muon-neutrino telescope were evolved more than twenty years ago in a series of workshops dedicated to the DUMAND concept, and were later implemented in the Lake Baikal experiments (§2.2).

The deep-water detection of high-energy muon-neutrinos exploits three properties:

i) the directional correlation of the muon and parent neutrino trajectories to within 0.7º for E_ν>3TeV;
ii) the unique upward-going directional signature of muons from cosmic neutrino interactions w.r.t. the vastly higher muon background from cosmic ray collisions in the atmosphere. Upward-going muons can only originate from local neutrino interactions: the Earth filters out all other particles;
iii) the long range of muons in water and rock over the neutrino energy range of interest. Upward going muons may be generated far from the instrumented volume and still be detected.

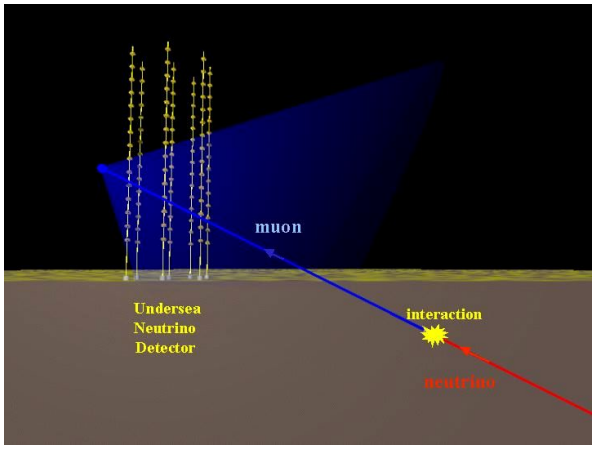

Fig. 1 Principle of detection of high energy neutrinos in an underwater neutrino telescope.

[+] member of the Antares Collaboration

Figure (1) illustrates the detection principle. Accurate reconstruction of the trajectory of a neutrino-induced muon relies on tracking over many tens of meters and measurement of the arrival time of the UV-blue component of the _erenkov wave-front to nanosecond accuracy on photomultiplier tubes (PMTs) whose positions are known to better than 22cm (equivalent to 1ns in water).

The choice of the PMT array spacing depends on the absorption and scattering length in the local deep-water environment, and to a lesser degree on the limit set by the chromatic dispersion in arrival time of the _erenkov photons. Due to the high purity of water at great depth, light absorption and scattering are small. However the detector is subject to backgrounds from cosmic ray muons, luminescence from deep-water creatures, and from _erenkov light from the β disintegration of ^{40}K, present in sea salt. Only the Lake Baikal freshwater site is free of ^{40}K background.

(2) Sites for underwater neutrino observatories

(2.1) Site selection criteria

The optimum site criteria for an underwater neutrino observatory are;

i) closeness to the coast to ease deployment and reduce the expense of the power and signal cable connections to the shore;
ii) as great a depth as possible to reduce background from atmospheric muons, and to suppress their misreconstruction as upgoing. As an example the Lake Baikal array at -1100m has identified 34 upgoing muons from a sample of 5.3 10^7 events [2] - in good agreement with MC predictions: at -4000m however, the flux of down-going muons is smaller by a factor ~80;
i) good optical properties in water long absorption [>20m] and scattering [~50m] lengths[1] for light in the range [$350 < \lambda < 550$nm]);
iv) low level of bioluminescence;
v) low rates of biofouling (bacterial film deposition and marine life accretion) on optical surfaces;
vi) low rates of sedimentation (for any upward-looking optical components);
vii) low velocity bottom current (~few cms^{-1} max.), since bioluminescence and sedimentation are dependent on this parameter.

The sites and layout of present and near-future underwater neutrino observatories are now considered.

(2.2) The Lake Baikal site and array

Experimental activity at the Lake Baikal freshwater site [figure (2)] spans a period of almost two decades[2]. The present ("NT-200") detector, in operation since 1998, has an instrumented volume rising from a depth of 1.1km, around 3.6km from the shore near the Southern end of the lake. It contains 192 PMTs in 96 coincident pairs attached along eight lines supported from the spokes and center of a heptagonal umbrella-like composite frame [figure (3)]. Each line is divided into "stories" containing two pairs of spherical optical modules separated in height by 6.25m. A fifth glass sphere holds the readout electronics of each storey.

Water transparency at 480nm is characterized by absorption (scattering) lengths of 20-24 m (30-70m) [2]. The high sedimentation rate at the site has necessitated the protection of upward-facing optical modules.

An extension to the detector ("NT-200+") has been approved to equip three additional lines of 6 pairs of optical modules at distances of 100 m from the center of the NT-200 array[2]. Commissioning is planned for spring 2004, and will enhance the fiducial volume to 0.01km^3 for neutrinos with energy above 10^{14}eV. The resulting detector will be considered as a prototype module for a 1km^3-scale detector.

(2.3) The Nestor site and array

The Nestor array will be located near Pylos on the Greek Ionian Sea coast [figure (4)]. An electro-optical cable has been laid from a shore station at Methoni to a site at - 4100m around 15km from the shore. The array, shown conceptually in figure (5), will comprise a series of 'towers', each rising 360m from a seabed anchor, held in tension by an underwater buoy. Each tower will contain 144 PMTs mounted on 12 titanium-framed 32m diameter 'floors' in the form of six-pointed stars. A pair of PMTs will be mounted on each arm, one looking up, the other down. The array is intended to be installed and extended without the need for underwater electro-optical connections by submarine vehicles. The water in this region of the Ionian basin is very clear, with ~ 55m attenuation length [3] for blue light. Bottom currents have been measured to be below 10cms^{-1}. Extremely low rates of sedimentation and biofouling permit a significant number of upward-looking optical sensors.

[1] The absorption coefficient a is defined as $1/L_a$; the scattering coefficient $b=1/L_b$. Their combination, $c = (L_a+L_b)/(L_a.L_b)$, is the attenuation coefficient. Due to the combination of absorption and scattering phenomena, light intensity scales with distance L as $I = (I_0 /L^2)\cdot e^{-cx}$.

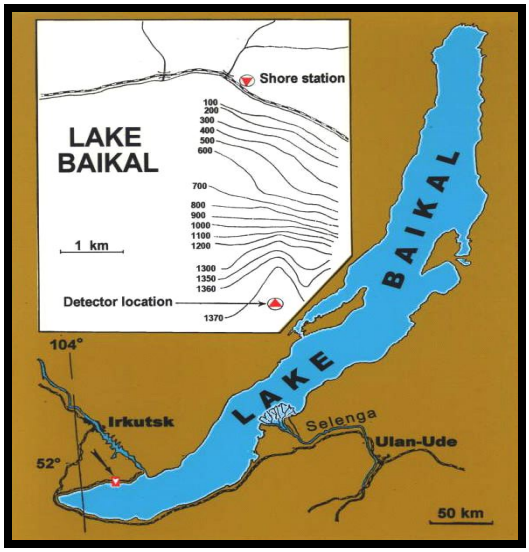

Fig. 2 The Lake Baikal site

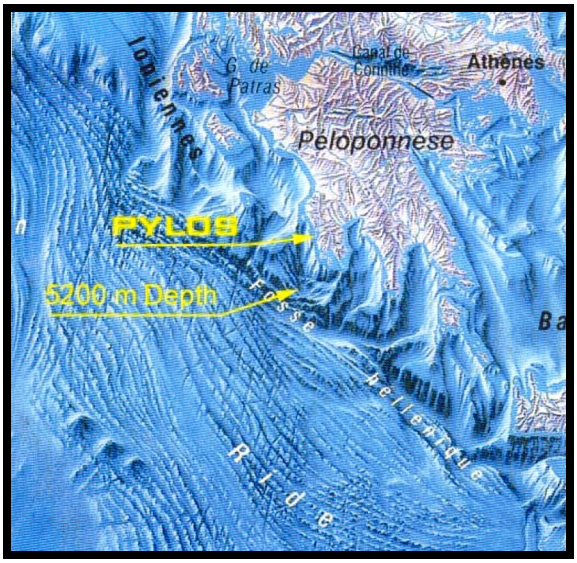

Fig. 4 The Nestor site in the Ionian sea

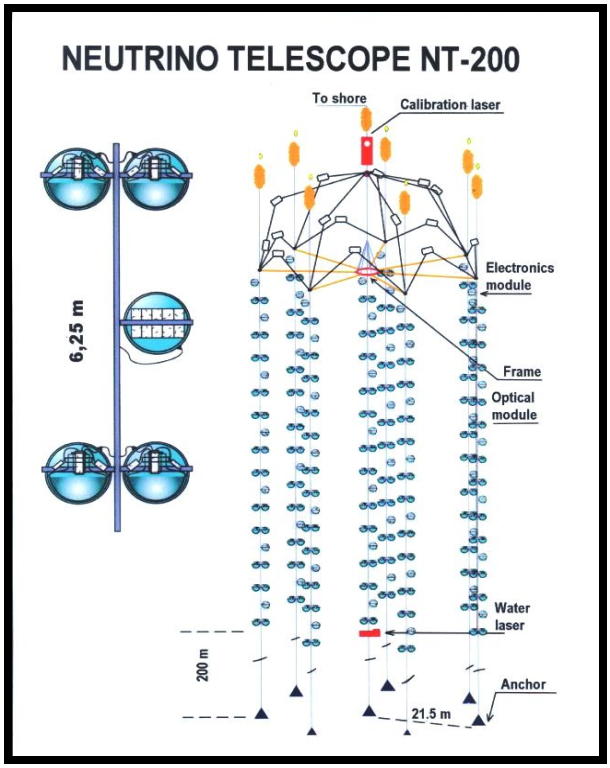

Fig. 3 The Baikal NT-200 array

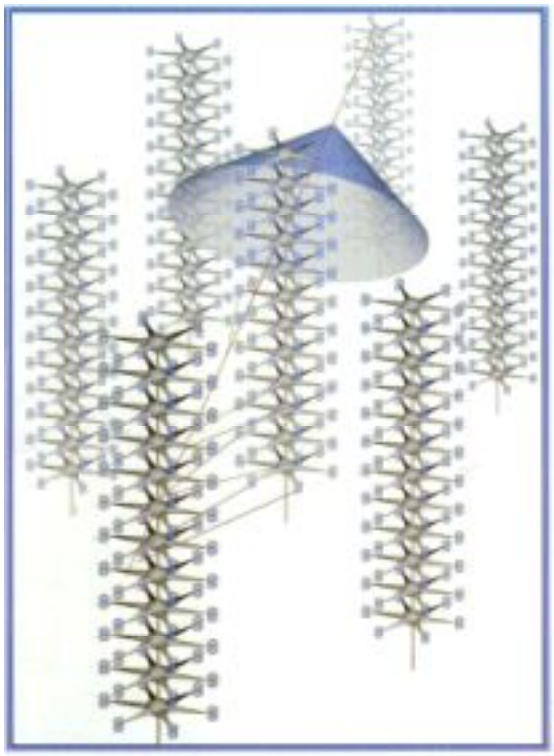

Fig. 5 Conceptual layout of the Nestor array

The Nestor cable to shore was deployed in June 2000, but was damaged by the ship during the cable lay. In January 2002 the end of the cable was recovered; the cable was repaired and redeployed at 4100m with an electro-optical junction box and associated instruments including an underwater current meter, an ocean bottom seismometer, a nephelometer to monitor light scattering, temperature and pressure sensors, a compass and a tilt-meter. Instrument data have been transferred to the shore for nearly a year; the first long-duration real-time data readout from a component of deep-sea neutrino detector.The planned deployment of the first detector floor in late 2002 was prevented by the onset of bad weather. The collaboration hopes to do so soon. This set up will collect data and evaluate detector performance in

real conditions over a long period. Following this engineering run, a detector consisting of four floors will be deployed in spring of 2003 for more tests and physics data taking. The deployment of a full tower is foreseen during 2004.

(2.4) The Antares site and array

The Antares collaboration is constructing, with the participation of part of the Nemo collaboration, a 0.1 km^2 aperture array for operation at –2400m off the French Mediterranean coast near Toulon [figure (6)]. The detector is linked to a shore station at La Seyne sur Mer by a 40km electro-optical undersea cable[2] laid in October 2001. The cable was terminated in December 2002 with the deployment of the central electro-optical junction box. The array layout is shown conceptually in figure (7). The first phase detector implementation will have twelve detection lines spaced on a 60m sea floor grid, anchored to the seabed and tensioned by submerged buoys. The array will contain a total of 1080 PMTs housed in optical modules (§3.1), grouped in triplets at 30 levels rising from -2300m to -1950m.
A series of site evaluation campaigns has been carried out by the Antares collaboration [4,5]. At the array depth of 2400m, the expected background rate from atmospheric cosmic ray muons is around 30Hz. This rate is insignificant in comparison with the ^{40}K β background from sea salt, which adds a singles rate of 60kHz to each 10 inch PMT, or with occasional bio-luminescence [figure (8)], which can peak during short bursts up to MHz rates, and is seasonally and ocean current dependent. Since the PMTs in the Antares array will be angled 45° downward toward the seabed, fouling is not a serious problem. The combined signal loss due to bio-deposition and sedimentation has been measured [4] to be less than 2% per year.

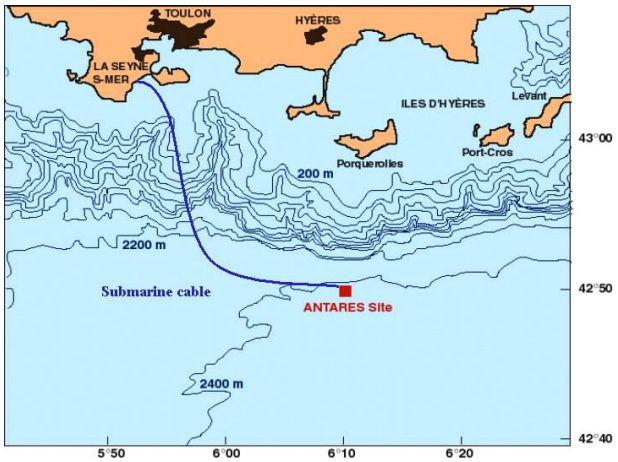

Fig. 6 The Antares Mediterranean site

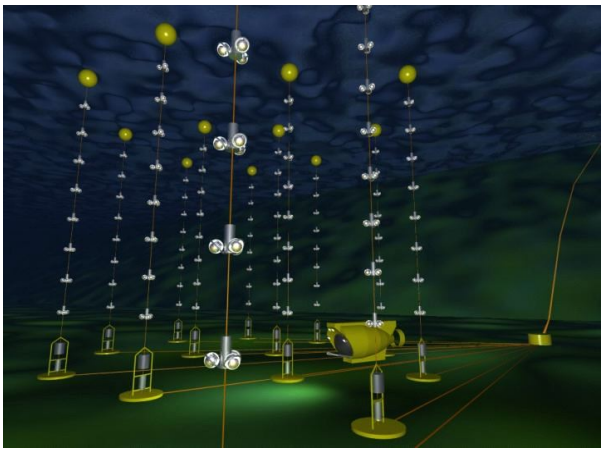

Fig. 7 Artist's impression of the Antares underwater neutrino detector array

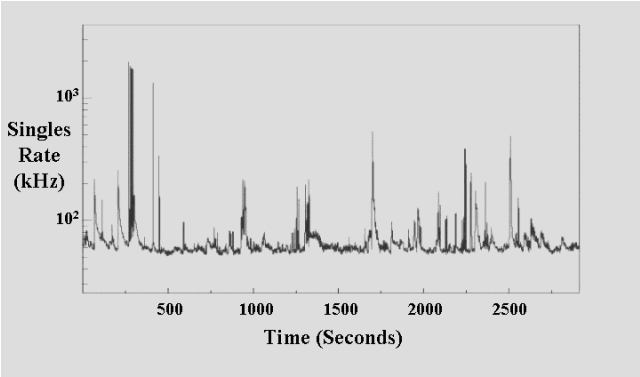

Fig. 8 Background singles counting rate in a 10 inch PMT at the Antares site.

The attenuation and scattering lengths in water at the Antares site have been measured in several campaigns between 1998 and 2000. At 466nm, attenuation [scattering] lengths have varied between 45 and 60m [37 and 79m]. The

[2] Manufactured and deployed by Alcatel

seasonal variation in these figures is significant, and the Antares array will incorporate an "instrumentation" line which will deploy underwater instruments including transparency and current profile monitors.

The construction of optical modules for twelve detection lines is well advanced. The commissioning of a full readout chain is progressing; a pre-production "sector line" of five optical module triplets was deployed in late 2002 following the deployment of the electro-optical junction box. A site instrumentation line will be deployed in early 2003. The commissioning of a 0.1km^2 array of twelve detection lines is planned for completion in 2004/2005.

(2.5) The Nemo site and array

The Nemo collaboration has identified a possible site for a km^3-scale array at –3500m a distance of 80km from the Sicilian coast near Capo Passero. [figure (9)]. At this location in the Ionian sea, bacterial concentration is relatively low, with the consequent advantages of low expected bioluminescence background and biofouling rate. Preliminary studies over a period of 40 days have shown no evidence for biofouling. At the site, the light attenuation (absorption) length exceeds 35m (70m)[6]. The average bottom current is around 3cms^{-1}, with a measured sedimentation rate of ~20mgm^{-2}day^{-1}. It remains to be proven that this low rate would not seriously degrade the performance of upward-looking PMTs after ~ 1 year, should the detector design include them.

The Nemo concept is for a 1km^3-scale array with 4096 optical modules hung from 64 "towers" laid in a square grid with 200m spacing. Each tower [figure (10)] would rise 750m from a seabed anchor, and would contain 16 "floors" separated in height by 40m, each with a pair of PMTs at each end of a 20m composite support arm. A matrix of support cables would ensure that successive floors deploy orthogonally under the force of the suspension buoy

.

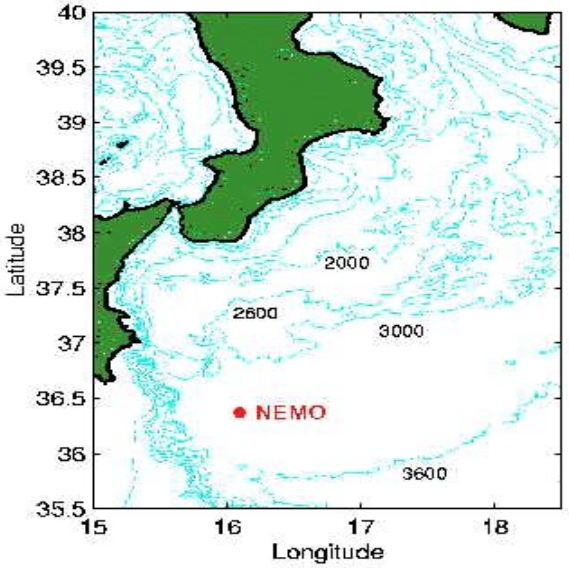

Fig. 9 The Nemo site South-East of Sicily

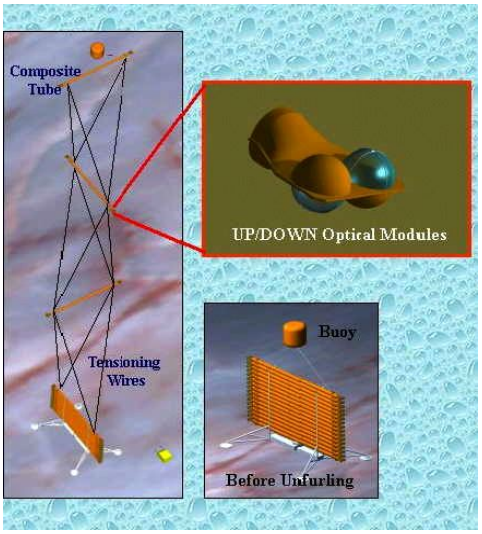

Fig. 10 Concept for a Nemo tower
(Courtesy N.Musumeci, INFN-LNS Catania

The Nemo collaboration has also brought into service a test site at a depth of 2031m. A 28km electro-optical cable from Catania in Sicily [7] splits 23km from the shore, a second brach running 5km to the "Geostar" underwater environmental platform. Each site is serviced by 10 optical fibers and 6 electrical conductors.

(3) Detector technology issues

In this section, the technology of underwater neutrino detectors is discussed in more detail.

(3.1) The optical detection modules.

As in existing water neutrino detectors such as Super-Kamiokande and SNO, _erenkov light will be detected using PMTs with single photon sensitivity. The extreme pressure at the operating depths requires that the PMTs be housed in pressure resistant glass spheres. Such spheres are readily available in diameters up to 43cm with depth ratings up to 7000m from several suppliers[3] and may be purchased in a variety of glasses, including low potassium (low β activity)

[3] (1) Benthos Corp, North Falmouth MA 02556 USA; Benthos type 2040-17V used in Nestor
(2) "Vitrovex" ® by Nautilus Marine Service GmbH, D-28357 Bremen, Germany. Vitrovex type 8330 used in ANTARES
(3) "EKRAN" (Novosibirsk) and Vitrovex used at Lake Baikal

variants. Spheres are supplied as matched hemispheres and can be predrilled with electrical and pump-out penetrations. Leaktightness at high pressures is given by plastic deformation of the ground glass contact surfaces of the hemispheres: no "O" ring joint is used.

Figure (11) illustrates the components of a generic optical module of an underwater neutrino detector. In Antares [8] and Nestor [9], the pressure spheres from different manufacturers exhibit very similar character-istics: 43 cm diameter with 1.5cm thick, low activity (< 0.5% K content) borosilicate glass having n = 1.47 and transmission > 87% for $\lambda >$ 400nm. A PMT with single photon sensitivity is is shielded from the Earth's magnetic field by a two part mu-metal wire cage, and is mounted and optically coupled onto one hemisphere using an index matching gel[4].Since power consumption is critical in large detector arrays powered through very long shore cables, the HV bias for the dynode array is usually generated in a custom PMT base from a DC input, using a Cockcroft-Walton chain. A light flasher system consisting of a blue LED and pulser circuit may be added to monitor the PMT transit time, which can exceed 60ns in large photocathode PMTs. The pulser trigger signal is referenced to the detector master clock.

Table (1) illustrates the performance of the Hamamatsu R7081-20 10-inch PMT used by the Antares collaboration. Its performance is fairly typical of PMTs used in deep-water neutrino detectors. The Nestor collaboration uses the 15-inch Hamamatsu R2018-02.

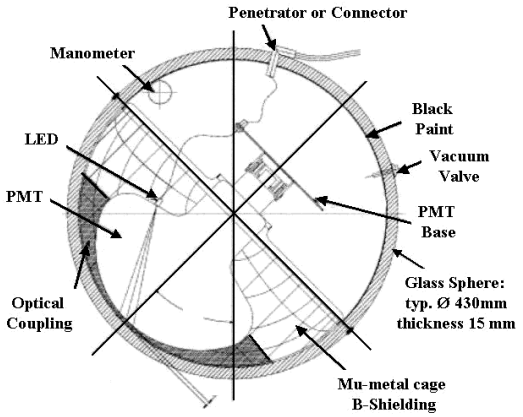

Fig. 11 A generic underwater optical module

.

Photocathode Sensitive area	$500cm^2$
Combined efficiency (quantum ⊕ collection: $400 < \lambda < 700$ nm)	> 16 %.
Gain @ 2500 V.	2×10^8
Pulse amplitude @ Nominal working gain of 5×10^7	60mV/50Ω
Transit Time	~ 60 ns
Transit Time Spread (TTS: FWHM)	< 3 ns
Dark count rate (@ 0.3 * single P.E. threshold)	< 10kHz.
Pulse Rise time	< 5 ns
Pulse Width (FWHM: single P.E.)	< 12 ns

Table (1) Parameters of Hamamatsu 7081-20 PM

The Lake Baikal collaboration adopted an innovative approach to the problem of cost of large PMTs[10,11]. In the 'Quasar 370' hybrid [figure (12); after [10]], a 370mm diameter external dome containing a photocathode and electrostatic focussing is used to generate and accelerate photoelectrons toward a disk of scintillator viewed by a small ("UGON") PMT. The device is sensitive to single photoelectrons and has a transit time spread in the range 1-2ns FWHM, competitive with large "monolithic" PMTs. A Quasar tube with a twin-anode PMT with a mesh dynode structure has been tested in the underwater array [12]. Inter-anode crosstalk was measured at 1-2%, and the muon sensitivity was comparable [12] to that of a coincident pair of single channel Quasar optical modules, [Figure (13)]. The collaboration has also developed a modification of the Quasar tube in which the scintillator and PMT are replaced by a semiconductor diode.

.

[4] In Antares: "Silgel" ® 612 A/B by Wacker-Chemic GmbH, 81737 Munich, Germany:
2-component silicon rubber, room temperature cure: n = 1.404. [transmission > 88% for $(400 < \lambda < 700)$ nm]:
In Baikal, (Nestor); Wacker Semicosil gel {n~1.4}, (gel or liquid glycerine {n=1.478}) with polyeurathane (gel) containment gasket.

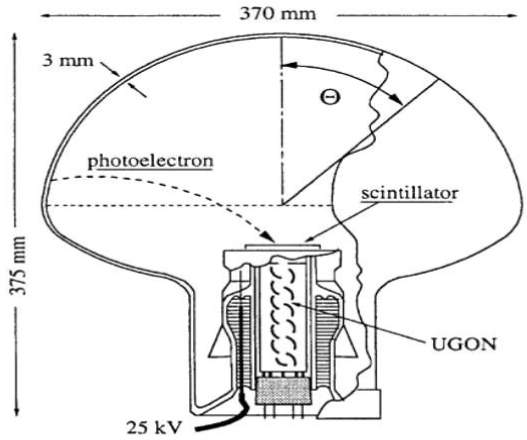

Fig. 12 Extended photocathode and electrostatic focussing dome used in the Lake Baikal array.

. . Fig. 13 Upward-looking Quasar-type optical modules from the Lake Baikal array. (Anti-sedimentation cones fitted.)

A group in the Nemo collaboration [13] is investigating a similar hybrid device [figure (14)]. The dome features a Sb-K-Cs photocathode and 25kV focussing field onto a disk of YSO crystal scintillator.

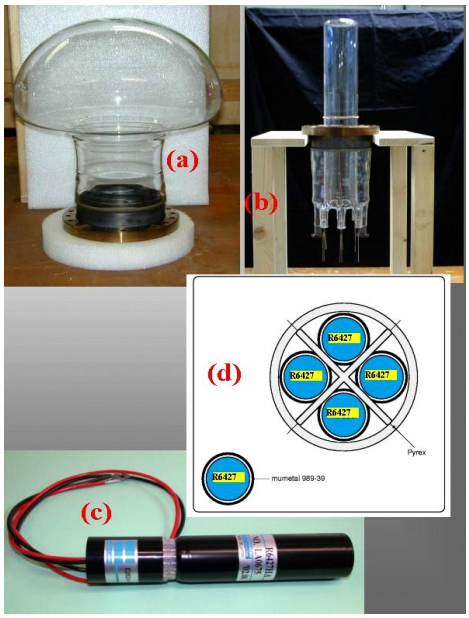

Fig. 14 A possible extension of the "Quasar" concept to multiple PMTs.
(Courtesy M.Battaglieri, INFN Genova)

The prototype is flanged together from two pieces (a), (b). Transit time (transit time spread) in the prefocusser are ~6ns (~1 ns). The incorporation of four miniature PMTs[5] [(c), (d)] would afford a degree of rejection of dark current and ^{40}K noise through local coincidence, together with a degree of directional sensitivity missing in most present generation optical modules.Other possible candidate photon detectors for optical modules include hybrid and avalanche photodiodes and **g**as **e**lectron **m**ultiplication devices (**GEM**s). Their potential for a km^3-scale detector must be evaluated.

[5] Hamamatsu R6427 1 1/8": QE 27% @ 420 Nm ; G ~ 3 10^6 @ 1500 V, Rise Time ~ 1.7 ns, FWHM ~ 0.5 ns

(3.2) Structural and pressure components

In the present generation of deep underwater neutrino arrays, the requirements of pressure and corrosion resistance have predicated the almost exclusive use of glass and titanium for pressure vessels. Structural supports are in titanium or composites, which will offer important cost savings in km^3-scale arrays. Figures (15, 16, 20 & 25) illustrate the use of titanium in the Nestor and Antares optical module support frames, electro-optical junction box and triplet electronics housing.

Each 32m-diameter Nestor titanium floor frame [9, 14] will incorporate a central titanium sphere containing data acquisition, power conversion and monitor & control system electronics. The six arms are composed of folding 5m tubular frames as shown in figure (15).

Although uncoated ferrous-metal structures (including stainless steel) are unsuitable for use in deep-sea water, possible cost reductions relative to titanium might be achieved by decoupling the problems of pressure and corrosion resistance. Figure (17) illustrates a junction box being considered by Nemo [15] in which a main electro-optical cable is split into parallel outputs for an array of detection lines. Cables exit the walls of the spherical steel pressure vessel through 'penetrators' and pass through an oil volume to terminate in underwater-mateable connectors arranged around the circumference of an oil bath built in composite GRP. An internal flexible water bladder[6] ensures the equipressure of water and oil by compensating the slight compressibility of the oil.

Fig. 15. Partially folded titanium frame of a Nestor 'floor' (at Nestor Institute, Pylos)

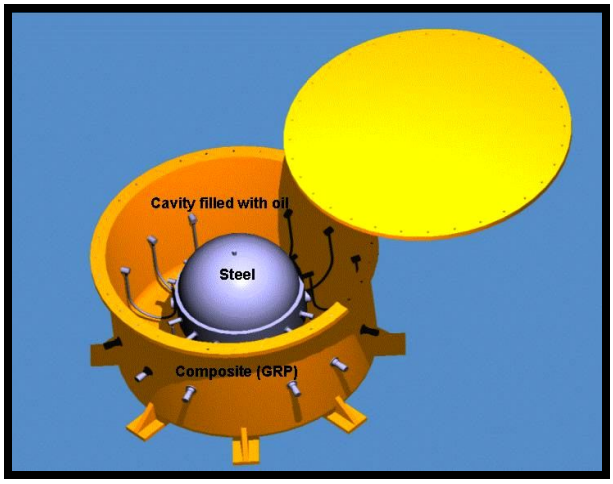

Fig. 17 Example of an oil barrier/steel deep-sea junction box pressure vessel
(Courtesy N.Musumeci, INFN-LNS Catania)

Fig. 16 Titanium optical module support frames for 'triplet' stories of the Antares detector

[6] Manufactured for example by Pronal SA 59115 Leers, France

(3.3) Bottom Anchors

The Lake Baikal, Nestor, Antares and Nemo underwater neutrino detectors tension their detection lines between anchors and a buoy, usually composed of a pressure (compression) resistant syntactic foam[7]. With the exception of the Baikal array, where detection lines can be winched onto the winter ice, bottom anchors for deep-water detectors are often sophisticated devices, incorporating an acoustic release system allowing the line to float to the surface for recovery. In this event a "disposable" deadweight is left on the seabed. In Antares and Nemo, an underwater mateable/ breakable connector[8] automatically disconnects with the unrestrained line buoyant force.

Fig. 18 Antares "Bottom String Socket" anchor

Figure (18) illustrates the recoverable part of the Antares anchor. This incorporates the detection line power converter **(a),** the acoustically activated release **(b)** the release shackle **(c)** and the acoustic survey system transponder[9] **(d)**. The disconnect speed of the underwater-mateable connector is regulated by a pair of sea-water dashpots **(e)**.

(3.4) Electro-optical connection and distribution

The present generation underwater neutrino arrays, and certainly a $1km^3$-scale array, will be deployed in stages on sites where an electro-optical shore cable has already been deployed. Unless terminating in deep underwater-mateable connectors, the shore cable must be dredged to the surface for connection to be made to it. Shore cables are deployed with dredging tails and acoustic transponders to enable them to be located for this operation. Options for the connection of additional detector lines are:

(i) underwater hook-up to the connector on the seabed anchor of a previously-deployed line, or more safely, to a previously-deployed junction box. Both require the use of underwater-mateable electro-optical connectors and a manned or **r**emotely-**o**perated submarine **v**ehicle (**ROV**);

(ii) deployment of each detection line with a dredge able or bouy-anchor released cable pigtail of length exceeding the water depth (4-5km). This allows a dry connection to be made at the surface with less expensive connectors, without the need for a ROV. The Nestor collaboration uses this option, and all its connections are made in air

[7] Glass micro-spheres in resin: manufactured for example by BMTI s.a. 83500 La Seyne sur Mer, France
[8] Mk II Hybrid (Electro-optical) Connector: Mfr: Ocean Design Inc, Ormond Beach, FL32174, USA
[9] Model RT861-B2T: Mfr: Oceano Technologies, 29200 Brest, France http://www.oceano-technologies.fr

before deployment. However, the seabed becomes cluttered with very long cables and their descent needs to be carefully controlled to avoid damage to the already-deployed detector;

(iii) previously-deployed detection lines are recover-ed (buoy-anchor captive release) for a dry daisy chain connection at the surface. No ROV required. Inter-line pigtails need to exceed the water depth. Cables and discarded anchors clutter the detector area. Considerable risk of damage to already-deployed lines.

Electro-optical distribution is a significant component of the cost of undersea neutrino detectors, particularly where the shore link cable is long or custom. In an effort to minimise this cost, Antares (Nestor) have deployed standard telecommunications cables with 48 (18) optical fibers and a *single* power conductor[10]. Figure 19 illustrates the (dry - mateable) electro-optical connector[11] of the Antares undersea cable. The connector shell is titanium with an outer diameter of 25cm. The four electrical contacts (in equipotential in the Antares cable) are grouped at the center. In both detectors, power returns to the shore station via a deep-sea electrode[12] and a shore electrode located below the

Fig. 19 Example of a commercial (Dry-mate) undersea cable electro-optical connector
(Photo courtesy Sea Con Inc.)

low tide level. Nestor uses monopolar DC while Antares will be powered with 4200V 50Hz AC at ~ 8A: a central transformer in an underwater junction box reducing and distributing the voltage to the detector lines. The major concerns with monopolar DC supply are the environmental impact of long-term underwater chlorine production and the effects of corrosion and chemical attack on nearby detector structures.

The Antares 50Hz distribution system is rather conservative: for a km^3-scale detector, R&D is required into distribution at 400Hz, as in aircraft systems, since this would allow the use of lighter and more efficient transformers. At the Nemo test site the main electro optical cable splits into two drops, each with 10 optical fibers and 6 power conductors [16], which will facilitate studies of a variety of AC and DC powering scenarios.

At the Lake Baikal array, the junction box is located over the detector. It is lifted every year during the winter ice season for recovery and repair of damaged components. All connections are performed on the ice before re-immersion.

Figure (20a,b) show the Antares central junction box, based on a 1m diameter titanium sphere with a central cylindrical connector belt through which enter the shore electro-optical cable, the sea electrode cable and 16 'penetrators' with 2.5m electro-optical cable pigtails ending in underwater-mateable connectors. The junction box is

[10] In long undersea telephone cables, optical signal repeaters are often wired in series through the single power conductor: one (the other) end station supplying a +ve (-ve) voltage w.r.t. the sea.
[11] Mfr: SeaCon/ Inc, El Cajon CA92020-1874, USA.
[12] In Antares via a 40mm diameter Titanium bar anode: length 1.7m, with "KERAMOX®-MMO" coating. Mfr: Magneto Special Anodes BV, 3125 BA Schiedam, Netherlands

installed in a titanium frame providing strain relief for the re-descent of the shore cable. The frame also contains an acoustic transponder[13] to locate the junction box following deployment. Figures (20a, 21) illustrate the Ocean Design MkII Hybrid connector receptacle[14]. The receptacle and cable mounting plug are oil-filled, with conductors and fiber ends shuttered in the oil volume in the unmated condition. Upon connection, the shutters open and oil is displaced into bladders at the rear of the receptacle and plug.

Fig. 20a Antares junction box with penetrators and underwater-mateable connectors

Fig. 20b Antares junction box during deployment; illustrating acoustic transponder (top) titanium support frame and undersea cable attachment.

The Antares junction box is the underwater hub of the detector, splitting the power between the detector lines, distributing clock signals and gathering the data signals from the detector lines onto the shore cable. Its 24kW transformer has sixteen separate 500V secondaries to power and galvanically isolate each detection or instrumentation line. Each output may be switched on/off or reset by a remotely controllable circuit breaker handled via the triply redundant junction box slow control system [figure (22)]. Passive fiberoptic splitters distribute the master clock signals in duplicate to the sixteen output lines. Lines will be connected to the junction box as they are deployed, using a ROV equipped with a manipulator arm.

[13] Model ET861T by Oceano Technologies: 9kHz Ë 14kHz & v.v.

[14] Mk II Hybrid Connector, Titanium shell: (2 conductors, 4 fibers). Fiberoptic insertion loss <0.2dB, HV standoff (pin-shell) 500V unmated, 1000V mated. Mfr: Ocean Design Inc, Ormond Beach, FL32174, USA Rated > 100 insertions < 6000' depth before oil refurbishment.

Fig. 21 Hybrid underwater-mateable connector receptacle by Ocean Design Inc.

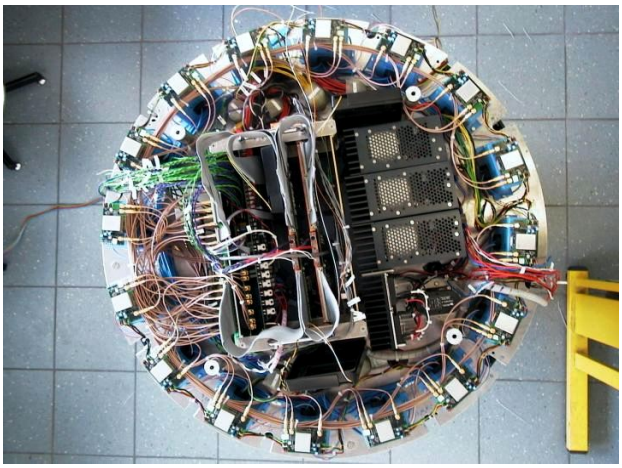

Fig. 22 Upper compartment of the Antares junction box: slow control cards, output circuit breakers and current monitors.

Power arriving at a detection line from the junction box is converted from 500V AC to 380 V DC at the anchor [figure (16)] for passage up the cable to the thirty electronics containers. In these, it is further reduced via DC/DC converters for use in optical modules and readout electronics. Very high reliability is required of critical underwater electronics and power distribution components, [MTBF (mean time between failures) >> 10 year typical operational life], due to the very high cost of recovery and repair of damaged components, particularly should submarine vehicles be required.
In contrast to the situation with electro-optical connectors, a wider variety of underwater all-electrical or all-fiber connectors exists.

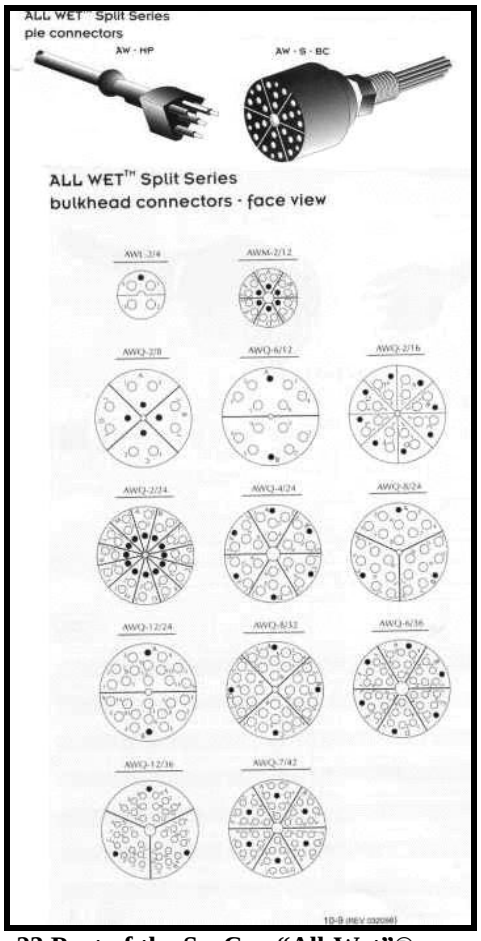

Fig. 23 Part of the SeaCon "All-Wet"® range of dry-mated underwater electrical connectors

Relatively inexpensive dry-mateable types for 500 bar + ambient pressure are available from several manufacturers. Figure (23) illustrates the "All-Wet" ® all-electrical series from Sea-Con Inc. The Nestor collaboration utilises connectors from the Gisma[15] ranges.

(3.5) Readout systems

(3.5.1) General

The principal problem for the readout systems of undersea neutrino telescopes is the time-stamping and separation of **s**ingle **p**hoto**e**lectron (**SPE**)-like PMT signals along muon trajectories from background due to ^{40}K disintegrations and PMT dark current pulses and occasional bioluminescence. Bioluminescence pulses, due to their very large signal size, require considerably more bits to timestamp and digitise. These pulses often represent the main contribution to PMT dead time, but are usually correlated over only a few adjacent PMTs.

Data may be uploaded to the shore with or without the application of local ("off-shore") triggering or local bioluminescence-rejecting coincidences. The "all-to-shore" option allows trigger decisions to be taken in on-shore electronics which can be upgraded to profit from technology advances during the lifetime of the detector.

(3.5.2) The Baikal data acquisition system

The Lake Baikal detector readout system is centred on local coincidences between adjacent optical modules [10], which reduce the combined dark current and bioluminescence noise rate to 100-300Hz per coincident pair. The array has a single photoelectron background uniformly distributed in time, allowing the use of a less sophisticated data acquisition system. Signals from locally coincident PMTs are sent to an array trigger module and junction box sited above the detector [figure (3)] in which an overall trigger is formed and from which timestamps and digitised amplitudes are sent via wire cables to the shore. Due to the low rate, a simple muon trigger signal (e.g. ≥ 3 or 4 local coincidence hits within the array in a 500ns window) [2] gives a sample nearly free of accidental coincidences.

(3.5.3) The Nestor data acquisition system

The Nestor readout [14] and data acquisition system (RDAQ) follows a data-driven architecture with waveform capture and capabilities for forming local (per floor) coincidences to reduce on-shore processing requirements.

Within the central titanium sphere of each floor, a "floor board" implements PMT pulse sensing, majority logic event triggering, waveform capture and digitization for 12 PMTs. The board extracts data, formats events and transmits data via the single bi-directional optical fiber up/downlink per floor to the shore. Its FPGA/PLDs can be reprogrammed through the downlink.

The heart of the board is the four-channel "Analog Transient Waveform Digitizer" (ATWD) ASIC, developed at LBNL. Each channel contains 128 10-bit ADCs, which after activation simultaneously digitize 128 samples of a selected channel. At the chosen sampling rate of 282 MHz, each channel has a time range of 453 ns. One channel in each ATWD is retained for synchronization, digitizing the waveform of a 40MHz clock signal. A "shore board" at the shore counting room, broadcasts a global 40 MHz clock signal via downlink to the floor board, receives the uplink data and transmits them to the second level triggering system.

A "floor-trigger" occurs when the programmed local coincidence requirement is satisfied on the floor. The time-stamp of a floor-trigger is defined as the leading edge of the majority logic signal, and the occurrence of such a trigger initiates waveform capture by the ATWD. This time stamp will also be used at the shore to build a global event combining experimental information from several floors.

The performance of the RDAQ electronics and the online software has been extensively studied in the laboratory using an LED calibration system. The robustness of the system has been demonstrated under near-realistic immersion conditions at the Nestor Navarino Bay Test Station. The rms time stability of ATWD sampling at frequency of 282MHz has been measured to be 6.4ps[14], negligible compared to the sampling period of 3.54 ns.

(3.5.4) The Antares data acquisition System

In the Antares array, the functions of the detector readout system are to time stamp (accepted) analog PMT signals, to digitize their charge, and to merge the data from the ninety PMTs on each detector line onto each single fibre-optic uplink to the shore station. The first stage of PM signal processing is performed by the Analog Ring Sampler ("ARS") ASIC {[17]; figure (24)}. The six ARS chips associated with each optical module triplet (two per PMT), are housed in

[15] Mfr: Gisma D-24539 Neumuenster, Germany: http://www.gisma-connectors.de

a common electronics container [figure (25)] together with (depending on the position of the triplet along the detection line), the compass and tiltmeter and/or hydrophone signal processing cards of the line positioning system (§3.6.2).

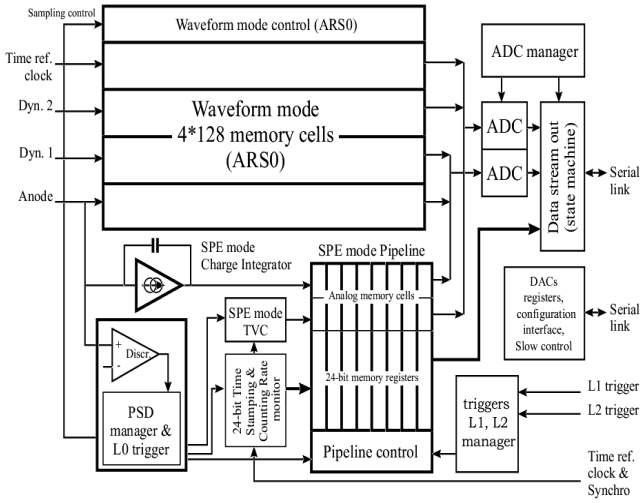

Fig. 24 Antares Analog Ring Sampler functionality

Fig. 25 Local electronics container (titanium) for the three optical modules of an Antares "triplet"

The ARS ASIC is implemented in AMS 1.2 μm CMOS technology, and is based on a four-channel mixed analog/digital pipeline memory. The ARS also implements a waveform shape-sensitive discriminator to distinguish single photoelectron-like ("SPE") pulse shapes from superimposed pulses or from larger pulses characteristic of background. The PMT direct anode signal enters one of the four inputs. Although each input can handle pulses up to 4.5V, an attenuated anode signal, and a signal from the 12th dynode are used to extend dynamic range in the case of large signals. The distributed 20MHz master clock signal enters the fourth input. A signal from the PMT anode triggers the ARS by crossing an amplitude threshold set to a fraction of the SPE average amplitude (the L0 threshold). The signal is time-stamped and its charge integrated to a precision of ~10% to compensate for time walk effects. A time to voltage converter (TVC) interpolates between 20MHz clock pulses to give a time resolution of ~ 0.4 ns. Integrated charge and timestamp are then stored in the mixed analog/digital pipeline memory. At the ARS output, an SPE tag consists of a header (1 Byte), the integrated charge (1 Byte), TVC (1 byte) and the time stamp (3 Bytes).

In recent tests [18,19] with signals from a PMT illuminated with mainly single photoelectrons at a single point on the photocathode, a time resolution of ~ 1.1ns has been achieved, comparing favourably with the PMT TTS of σ ~1.3ns with full photocathode illumination. The intrinsic time resolution of the ARS was determined to be σ ~ 350ps from measurement of the separation of two pulses injected into the ARS with a known time difference.

Analog pulse shape discrimination separates SPE pulses, which are charge integrated, from "waveform" (WF) pulse shapes, which are waveform-sampled in 128 samples at up to 1 GHz. This processing is implemented when the pulse height exceeds several photoelectrons, when the time over the L0 threshold is longer than normal, or when the L0 threshold is crossed more than once in the charge integration time. With 128 analog samples of the waveform, at the ARS output, a WF event can typically contain > 250 bytes.

SPE events are expected to represent more than 98% of the Antares data, while WF events will be mainly generated by background phenomena, primarily ^{40}K disintegrations and bioluminescence. The pipeline memory of each ARS can store up to 16 SPE hits or 4 WF hits.

With a singles rate of 70kHz, and 2% fraction of WF events, the (typical) data rate will be ~7Mb/s per PMT. Two ARS chips are connected to each PMT to reduce dead time. This data rate is shared between the (fast) output ports of the two ARSs and is well within the 20Mb/s bandwidth limit of each. The PMT readout system is intended to handle an average singles rate of up to 100kHz with surges of up to 250kHz due to bioluminescence bursts.

Data from five PMT triplets (five levels) will be merged onto a single descendant fiber with a typical bandwidth of 105MB/s. Data from six such fibers will be DWD[16]-multiplexed onto a single fiber at the bottom of each detection line,

[16] "**D**ense **W**avelength **D**ivision"

resulting in a typical data rate to shore of 700MB/s per line. These fibres pass through the junction box and onto the 40km electro-optical cable linking the detector array to the shore

An on-shore data switchyard will de-multiplex up to 70 incoming data streams and pass data to a processing farm consisting of up to 100PCs running at an input data rate in the range 50-100MB/s.

(3.5.5) Nemo readout system R&D

The Nemo collaboration is studying a readout system for a km^3-scale array of 4096 PMTs. An event rate of 50kHz per PMT (dark current + 40K + SPE signals + average bioluminescence contribution) has been assumed [16]. A PMT signal-processing ASIC ("LIRA01", built in AMS 0.35µm CMOS technology: [16]) with 3 channels of 256-deep switched capacitor array analog memory and 200MHz sampling rate is under development. The ASIC channels sample the PMT anode, a dynode and the 20MHz master clock. LIRA01 will also incorporate a twin threshold (0.25SPE, 5SPE) discriminator trigger and single photon classifier. The ASIC is aimed at a temporal resolution of 300ps. The DAQ output rate (after zero suppression and packing) is ~$5Mbs^{-1}$ per PMT. Two LIRA ASICs will be used in each optical module: while one is sampling the PMT, the other will push data out towards a 20MHz sampling ADC.

A "**s**ynchronous **d**igital **h**ierarchy" (**SDH**) protocol is being considered for data transmission and reception. An STM-1 tributary: (up to 155Mb/s) might be used for the readout of a floor (4 PMTs) onto a single descending optical fiber. In electronics at the tower base, the 16 floor STM-1 streams would be multiplexed onto a single optical fiber running the STM-16 protocol (up to 2.5GB/s).

The array power and readout architecture envisions 8 secondary junction boxes (SJBs) and a primary junction box (PJB) to which the shore electro-optical cable is connected. The principal data paths from the SJBs to the PJB follow a star network, with a redundant data ring between the SJBs. Data from each sub array of 8 towers would be DWD-interleaved[17] in its SJB onto a single optical fiber, thence passing to the PJB (with the additional redundant highway between SJBs), before being retransmitted onto the 100km shore electro-optical cable following a +17dBm amplification[18].

(3.6) Underwater acoustic survey and navigation

The reconstruction of muon tracks in an underwater neutrino detector is based on precise measurements (~1 ns) of the arrival times of _erenkov photons at optical modules. This reconstruction requires knowledge of the positions of the optical modules relative to each other, or more practically, with respect to fixed reference points such as the detector line anchors. The precision of this spatial positioning should be better than the corresponding dispersive uncertainty in the arrival time of _erenkov light detection (e.g. ~1.6 ns over a typical flight distance of 40m in Antares). Since 1 ns is equivalent to 22cm of light travel path in water, the relative position of every OM should be known to ~ 10-20cm.

Since detection lines will be suspended between sea anchors and submerged buoys subject to movement by deep ocean currents, the positions of individual optical modules will need to be regularly determined from measurements of line curvature and twist. In Antares, the relative positions of the OMs will be obtained from fits to position data determined by two independent systems: a high frequency **l**ong **b**ase**l**ine (**LBL**) acoustic system [19,20] and a series of semiconductor tiltmeter-compass sensors disposed along each detection line. The relative positions of the OMs will then be deduced from this reconstructed line shape and from the geometry of the OM frame. Additionally, a network of laser and LED beacons producing narrow, timestamped blue light flashes will be used to give redundancy in the on-line calibration of PMT timing.

(3.6.1) The Antares acoustic positioning system

An array of four 40-60kHz acoustic transponders [20] [19][figure (26)], delineating a 300 x 300m LBL square, has been deployed on the seabed at the Antares site. Additional transponders will be added (on sea achors) as detection lines are deployed. The LBL transponders will transmit sound signals to hydrophones mounted at six positions (altitudes 100, 184, 256, 328, 388 & 448m) along each detection line. The 3D positions of the hydrophones will be obtained by triangulation. The sea bed transponders will interrogate each other and the seabed anchors to determine their relative positions.

[17] Candidate device: AWG/CI008 by E-Tek Dynamics
[18] Candidate device: type 1738U Erbium-doped Fiber Amplifier by Agere Systems
[19] Mfr: Genisea/ECA, 83078 Toulon, France: Frequency range 44-60kHz, 2kHz channel spacing

Fig. 26 Deployment of the acoustic transponders of the Antares long baseline survey system

Figure (27) illustrates a recent implementation of the acoustic survey system with rangemeter hydrophones at three elevations on a deployed line. The precision of vertical height measurement between two hydrophone rangementers was measured to be better than 5cm [figure (28)]. The transmission and reception of each sound pulse must be time-referenced relative to the master clock signal used to time stamp PMT data. The conversion of acoustic transit times to distances requires accurate knowledge of the sound velocity within the detector. This in turn depends on the temperature, salinity and pressure [21]. Instrumentation to monitor these parameters will be needed, and has been extensively studied in the Antares-Nemo collaboration. These instruments are included on a dedicated instrumentation line.

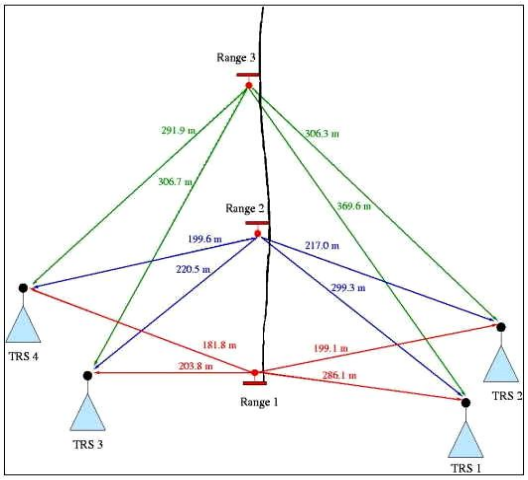

Fig. 27 Illustration of relative positions of hydrophone rangefinders and transponders

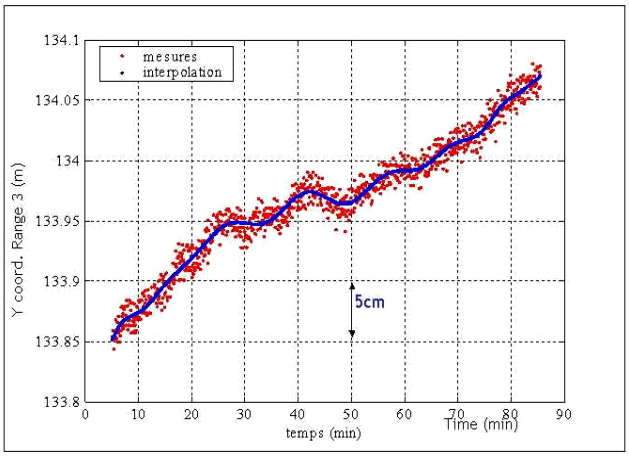

Fig. 28 Time variation of vertical displacement between hydrophone rangefinders due to deep ocean current

(3.6.2) Semiconductor tiltmeter/compass systems

The detection lines of Antares will incorporate combined bi-axial tiltmeter and compass sensors[20] [figure (29)] to give the local tilt angles of each OM triplet level with respect to the horizontal plane (range [precision]; ±20° [±0.2°] in pitch and roll), as well as its orientation relative to Earth Magnetic North (heading range [precision]; 0-360° [± 0.5Ë1°]), caused by cable torsion.

[20] Model TCM2-20: Mfr: Precision Navigation Inc., Santa Rosa CA95403, USA http://www.pnicorp.com

The performance of the positioning system has been studied in various configurations (varying the number of acoustic sensors and tiltmeters; the locations and precision of sensors, positions of missing sensors etc.), with differing values of deep water current and detector line twist as a function of altitude. These studies indicate that the proposed combination of acoustic triangulation and tiltmeter-compasses should allow the positions of all OMs to be determined with an accuracy $\sigma < 10$cm in deep water currents up to 15cms^{-1}.

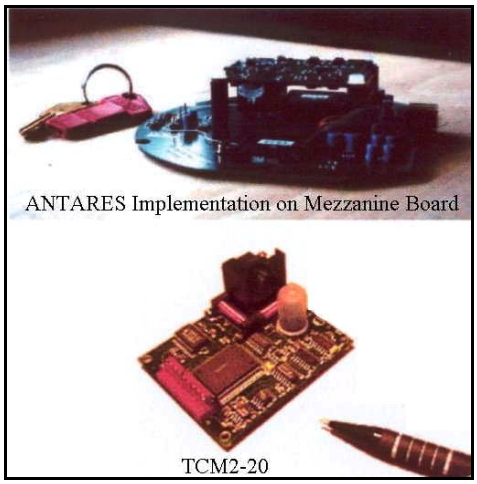

Fig. 29 Antares combined tiltmeter-compass card

(3.7) Site evaluation and underwater environmental instrumentation

Nemo, Lake Baikal and Antares have a common program of site measurements and instrument cross calibration [6,22]. Some instruments have been used at all three sites. Additionally, many of results from the instruments used in site characterisation are of interest to the oceanographic, deep-sea biology and geophysics communities. The Nestor collaboration has, for example, been acquiring real-time seismograph and ocean current data at its Ionian sea site since January 2002. The Nemo test site lab at Catania will acquire real-time data from the GEOSTAR-Poseidon underwater seismic station.

One output of the Antares junction box (2 conductors @ 500V AC, and 4 optical fibers; DAQ Tx, Rx and 2 carrying GPS-referenced clocks) will be made available for oceanographic collaborators, while on another output a comprehensive array of environ-mental monitoring instruments for the Antares site, some developed by the Nemo collaboration, will be incorporated onto a dedicated instrumentation line.

(3.7.1) The Antares instrumentation line

One of the sixteen junction box outputs will be reserved for an "instrumentation line" containing equipment for monitoring the detector array and deep-sea environmental parameters including salinity, sound velocity, water transparency and current profile. For detector-wide timing calibration, a laser beacon will illuminate the array with fast (900ps), time-stamped laser[21] pulses at a wavelength of 456nm. Its action will complement shorter-range blue LED beacons distributed among the detection lines.

[21] Incorporating a NG-10120-120 laser head.Mfr Nanolase, 38941 Meylin, France

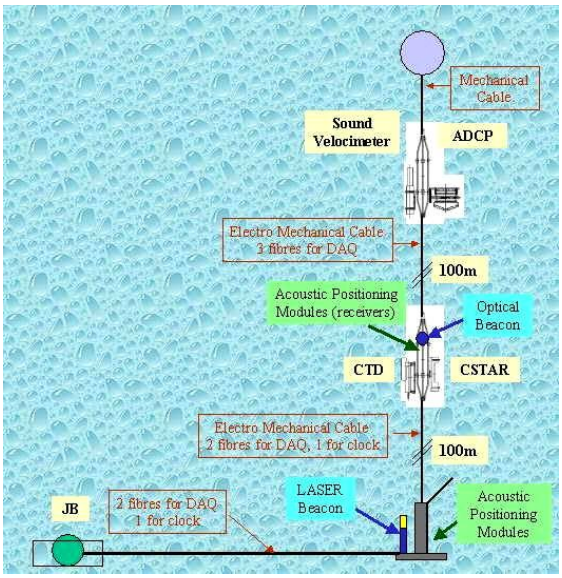

Fig. 30 Configuration of a prototype instrumentation line to be deployed at the Antares site.

The deep-sea current profile (velocity, direction) will be sampled over 256 intervals over the full detector depth of 300m by a pair of 300kHz acoustic Doppler current profilers[22] with a velocity range [resolution] of 5 ms^{-1} [1 mms^{-1}].

The optical attenuation of water at 470nm will be measured over a 25cm path length using a commercial photodiode-based water transmission meter[23]. The line will be equipped with sound velocity meters of the same type as installed close to the sea anchors of some detection lines. These devices[24] have a flight path of 20cm and a precision of $\pm$ 0.05ms^{-1} for typical velocities in the range 1400-1600ms^{-1}. Several velocity meters will also be equipped with conductivity-temperature[25] and depth (pressure) probes[26]. A seismometer will also be connected to the instrumentation line. A preliminary version of the instrumentation line with a single current profiler [figure (30)] will be deployed in early 2003.

(4) Acoustic detection of neutrinos

Several groups in Europe and worldwide are pursuing the acoustic detection of neutrino interactions. Very high-energy (~10PeV) neutrinos generate a cascade of secondary particles through e-m or hadronic showers produced in their interactions with water. Secondary ionisation induces local heating of the water, generating a corresponding pressure induced sound pulse, which may be detected (triangulated) with a sufficiently sensitive hydrophone (array). The production of a sound pulse is illustrated in figure (31).

Such acoustic detection would exploit the much longer attenuation length of sound, than light, in water. Sound pulses around 400m from a 10PeV cascade at a depth of 4km should give bipolar sound pulses with amplitude varying between 8 and 70µPa (depending on the theoretical model assumed), with duration in the range 60-80µs. By way of reference, the human ear is sensitive to sounds of ~25µPa @ 1kHz.

The Lake Baikal collaboration has installed a hydrophone [2] for use in correlating the arrival of extensive air showers with a surface (ice) scintillator array and the NT-200 underwater optical detectors. A group from the Nemo collaboration will install four hydrophones[27] at the Nemo test site near Catania [23].

Optical encoding of the hydrophone signals will take place at depth for transmission through the 28km shore cable with continuous data transmission at 96K * 24 bit samples per second.

[22] Workhorse Monitor; Mfr: RD Instruments, San Diego CA 92131 USA
[23] C-STAR by WETlabs Inc. http://www.wetlabs.com
[24] Mfr: Genisea, France: model QUUX-3A(A):
[25] OEM-OT sensor by Falmouth Scientific Inc., Cataumet, MA02534, USA http://www.falmouth.com precision ±0.001mScm^{-1}
[26] Mfr: Druck S.A., 92600 Asnières sur Seine, France
[27] TR4037 by Reson 1-80kHz, omnidirectional, 1VμPa^{-1}@ 250Hz : a custom development, 2500m depth rating

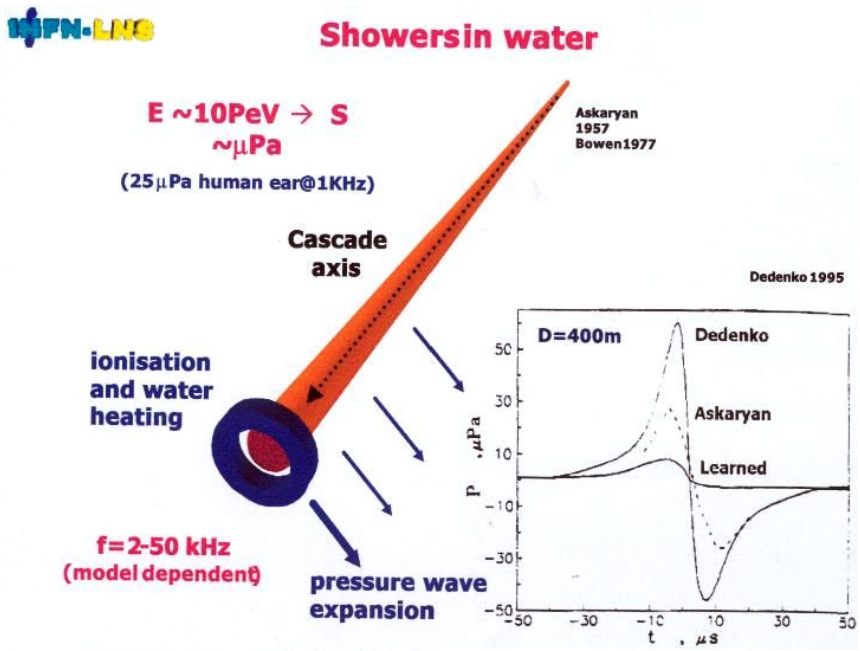

Fig. 31 Acoustic pulse formation by high energy shower associated with very high energy muon
(Courtesy G. Riccobene, INFN-LNS Catania)

The installation will be used for extensive studies of underwater noise, indispensable precursor data to determine whether high-energy neutrino-induced sound signals can be separated from the oceanic acoustic clutter. Additionally, this installation will have considerable interdisciplinary interest since it should be able to detect the passage of whales within a range of 10 miles, and of dolphins at larger ranges. A group from the Antares collaboration has begun studies of the readout of hydrophones in an existing array near the Antares site. It is further planned to mount hydrophones on two Antares detection lines.

Further afield, a program of study has begun at the **AGAM** submarine detection array near Kamchatka, which contains 2400 hydrophones in a (102 x 17.3 x 4.5) m array. Other tests will be made at the **AUTEC** (**A**tlantic **U**ndersea **T**est and **E**valuation **C**enter) 52-sensor array off the Florida Caribbean Coast.

(5) Deployment and recovery considerations

The Lake Baikal detector site allows deployment and recovery operations to be carried out from the winches deployed on the winter ice cover. Figure (32a,b) shows the deployment of elements of the NT-200 composite support frame during deployment. All electro-optical connections are made on winter ice before immersion.

Table (2a,b) illustrates the equipment necessary in the deployment of a scalable underwater array centred around a junction box linked to a shore cable. Connections of underwater detection lines are assumed to require the plugging of cables with underwater-mateable connectors through the use of a manned submarine or ROV. Table (2a,b) is based on the Antares experience. In all cases, an already-deployed seabed acoustic transponder net and a ship with a GPS-referenced dynamical positioning system are required. Objects to be deployed on the seabed are equipped with their own acoustic transponders, allowing their positions to be triangulated with respect to an already deployed acoustic transponder net, of which the Antares LBL is an example. During the deployment of the Antares junction box at a depth of 2400m, the undersea electro-optical cable was first located through shipborne interrogation of the acoustic transponder attached to its 400m long dredging tail. Movement of this transponder confirmed when the lowered grapple had succesfully snagged the dredging tail. The descent of the junction box to the seabed was monitored in real time by triangulation [figure (33)] of the position of its indivual acoustic transponder relative to the deployed net. In figure (33)

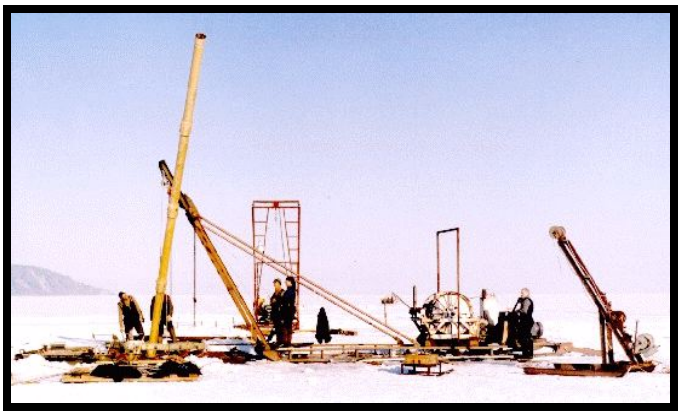

Fig. 32a,b Deployment of elements of the Baikal NT-200 support frame

Table 2a Deployment resources required

Deployed Object	Underwater resource required		
	Differentia lGPS/ Acoustic Nav	Grapple	Submarine Vehicle
Shore-Site E/O Cable+ transponde r	YES	NO	NO
Junction Box+ transponde r	YES	YES: For Shore-site E/O cable dredging tail	NO
Detection Line+ transponde r	YES	NO	NO
Line- JB cable connect	YES	NO	YES

Table 2b Recovery resources required

Deployed Object	Underwater resource required		
	Differentia lGPS/ Acoustic Nav	Grapple	Submarine Vehicle
Shore-site E/O Cable (for JB attachment)	YES	YES: For Shore-site E/O cable dredging tail	NO
Junction Box+ transponde r	YES	YES: For JB dredging tail	YES: Unplugging Line- JB E/O connection lines at JB
Detection Line (anchor abandoned on seabed)	YES	NO	NO Line E/O plug auto-disconnect
Line- JB E/O cable	YES	NO	YES

In figure (33) the most recent position of the junction box is shown by a rectangle, while previous positions (at differing heights) are indicated by red spots. During the descent, the dynamical positioning ship adjusted its position 2.5km along the track of the undersea cable as 2.5km of cable were re-laid on the seabed with the junction box attached.

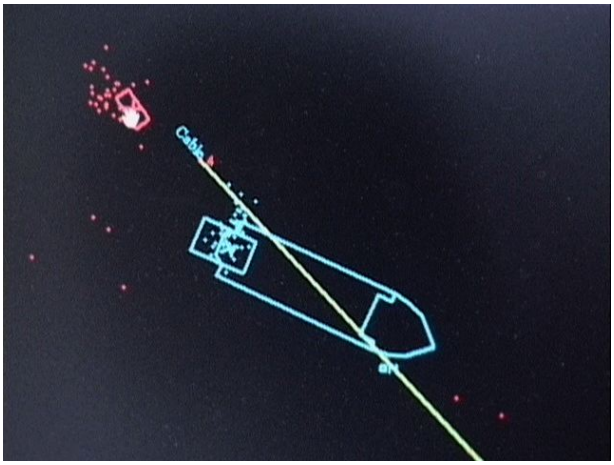

Fig 33. Acoustic transponder positioning of the Antares junction box during descent to seabed.

By contrast, the Nestor array will be deployed without the need for ROVs to perform underwater cable connections. Several times in tests the collaboration has deployed and recovered payloads composed of its base station and several floors from a depth of 4000m using cable-laying ships or platforms. The collaboration is constructing a highly specialised deployment platform. The self-propelled and ballasted platform [figure (34)] has an equilateral triangular form of side 51m, with a central well. It will be equipped with a GPS-related dynamical positioning system capable of maintaining its position at sea to a precison of several meters, and can be used to deploy structures with diameters as large as 100m.

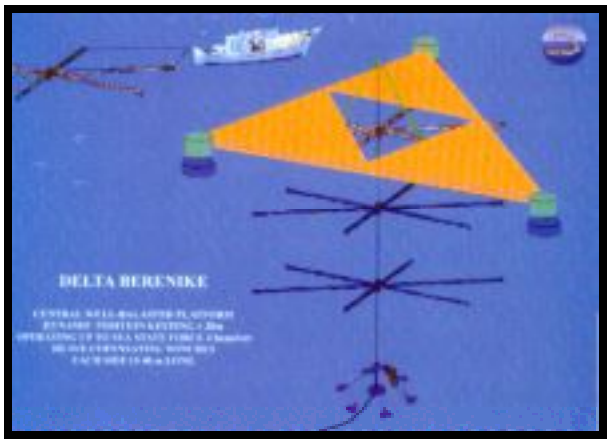

Fig. 34 Nestor deployment platform.

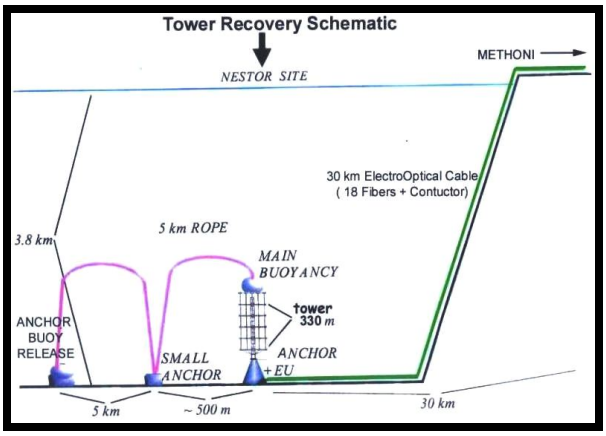

Fig. 35 Nestor tower recovery procedure.

Figure (35) illustrates the Nestor deployment/recovery concept [24]. Using a 5000m neutral buoyancy [“**Re**covery **Ro**pe” (**ReRo**)] rope, the Nestor tower is lowered to the sea bottom and the ReRo is laid across the sea floor with an anchor and buoy at its end. When the anchor is released with a coded acoustic signal the buoy floats to the surface and the tower can be recovered and raised to the surface by winching on the ReRo.

6) Conclusion and km^3-scale detector outlook

The Nestor and Antares projects have finished their underwater site evaluation and instrumentation development, and have entered the construction and deployment phase. The Nemo collaboration has established a test site near Catania and has identified a site at a depth of 3000m that appears suitable for a km^3-scale array. The Antares and Nemo collaborations are working together to build a first generation detector at the Antares site. Lake Baikal and Antares/Nemo have a common program of on-site measurements, while Lake Baikal and Nestor collaborate on various engineering issues.

The Lake Baikal, Nestor and Antares projects can be thought of as developmental platforms for a km^3-scale underwater neutrino array. They demonstrate that the technological building blocks for such a detector exist at the present time. However much R&D will be needed in the coming years to effect component cost reductions to allow the construction of a much larger Northern Hemisphere array. Some of this R&D has been started within the Nemo collaboration. The participation of industrial suppliers of telecom-munications equipment, undersea telecommunications cable and underwater-mateable connector technology, manufacturers and operators of submarine ROVs, and support vessels are all essential to the implementation of such a huge underwater assembly. The provision of space and services for undersea oceanographic, geophysical and deep-water biology instrumentation will be vital to the interdisciplinary appeal of such a project.

The development of acoustic detection systems, making use of the much longer attenuation length of sound in deep water might provide a useful adjunct to a km^3-scale detector, perhaps facilitating the search for ultra-high energy (>10PeV) neutrinos.

Acknowledgements

I thank my collaborators from the Antares and Nemo collaborations for their permission to quote from hitherto unpublished R&D, and to the Lake Baikal and Nestor collaborations for information, some unpublished, on that detectors.

References

[1] "High Energy Neutrino Observatories";
Report of the High Energy Neutrino Astrophysics panel to PaNAGIC Committee: HENAP REPORT 1-July 2002

[2] B. Lubsandorzhiev; "The Lake Baikal neutrino experiment: present status and future prospects":
Proc. 2002 Workshop on Ring Imaging _erenkov Detectors (RICH 2002), Pylos, Greece, June 2002,
to be published in Nucl. Instr. & Meth. A

I Belolapitikov et al; "The Baikal underwater neutrino telescope: design, performance and first results"; Astroparticle Physics 1997, Vol 7, p 263

[3] E. Anassontzis et al ; "Light transmissivity in the Nestor site": Nucl. Instr. & Meth. A 349 (1994) 242

[4] P. Amram et al; "Sedimentation and fouling of optical surfaces at the Antares Site"; June 2002,
submitted to Astroparticle Physics astro-ph/0206454

[5] P.Amram et al; "Background light in potential site for the Antares undersea neutrino telescope"; Astroparticle Physics 13 (2000) 127-136

[6] A. Capone (INFN-ROMA 1); "Nemo Activities on Site Selection and Characterization" Antares collaboration meeting, Catania, Italy 24-28/9 2002

[7] M. Sedita (INFN-LNS, Catania); "km^3 Cabling, connection and data transmission development" *ibid*

[8] P. Amram et al; "The Antares optical module"; Nucl. Instr. & Meth. A 484 (2002) 369

[9] E. Anassontzis et al ; "The optical module for the Nestor neutrino telescope": Nucl. Instr. & Meth. A 479 (2002) 439

[10] R. Bagduev et al; "The optical module of the Baikal deep underwater neutrino telescope" Nucl. Instr. & Meth. A 420 (1999) 138

[11] V. Balkanov et al; "Search for neutrinos from the core of the Earth with Baikal underwater detector NT-36":
Proc 25th International Cosmic Ray Conference, Durban, South Africa July28-August 8 1997: Vol. 7, p269

[12] B. Lubsandorzhiev ; "New developments of Photodetectors for the Lake Baikal neutrino experiment":
In press physics/0208008 2 Aug 2002

[13] M. Battaglieri (INFN-Genova); "Development of a hybid PMT", Antares collaboration meeting, Catania, Italy 24-28/9 2002

[14] S. Tzamarias et al: "Nestor: A deep sea neutrino telescope":
Proc. 2002 Workshop on Ring Imaging _erenkov Detectors (RICH 2002), Pylos, Greece, June 2002, to be published in Nucl. Instr. & Meth. A

[15] N. Musumeci (INFN-LNS, Catania); "Goals of mechanical development for km^3-scale detector", Antares collaboration meeting, Catania, Italy 24-28/9 2002

[16] L. Lo Nigro (INFN, Catania): "Technical solutions for the electronics and data transmission" *ibid*

[17] F. Druillole et al; "The Analogue Ring Sampler: An ASIC front-end for the Antares neutrino telescope":
Proc. IEEE Nuclear Science Symposium, 4-10 Nov 2001, San Diego, CA, USA

[18] F. Feinstein; "The Analogue Ring Sampler: a front-end chip for Antares"
Proc.3rd Baune Conference on new developments in photo-detection, Baune, France, June 17-21 2002; to be published in Nucl. Instr. & Meth. A

[19] G. Hallewell; "Status of the Antares underwater neutrino telescope"
Proc. 2002 Workshop on Ring Imaging _erenkov Detectors (RICH 2002), Pylos, Greece, June 2002, to be published in Nucl. Instr. & Meth. A

[20] V. Bertin, Genisea ; "Système de positionnement acoustique base longue: Description technique" Antares report 3INS0103B, May 2000

[21] C. Chen and F. Millero; "Speed of sound in sea water at high pressures,"
J. Acoust. Soc. Am., Vol. 62, No. 5, 1129-1135, Nov 1977

[22] J-P. Schuller (CEA Saclay); "Some Antares results from Common Campaign with Nemo"
Antares collaboration meeting, Catania, Italy 24-28/9 2002

[23] G. Riccobene (INFN-LNS, Catania); "A deep sea station for the on-line monitoring of acoustic noise at the Nemo test site." *Ibid*

[24] L. K. Resvanis: " High energy neutrino experiments" Proc. XII international symposium on very high energy cosmic ray interactions, CERN 15-20 July 2002 via http://www.nestor.org.gr/XII/index.htm